RSC Advances

PAPER

View Article Online
View Journal | View Issue

Cite this: *RSC Adv.*, 2025, **15**, 12342

Corrosion inhibition and *in silico* toxicity assessment of imidazo[1,2-*a*]pyrimidine-Schiff base derivatives as effective and environmentally friendly corrosion inhibitors for mild steel†

Mohamed Azzouzi, *[a] Walid Daoudi,[a] Omar Dagdag,[b] Avni Berisha,[c] Hansang Kim,[b] Abdelouahad Oussaid,[a] Abdelmalik El Aatiaoui[a] and Adyl Oussaid[a]

This study reports the synthesis and corrosion inhibition evaluation of two imidazo[1,2-*a*]pyrimidine-Schiff base derivatives (**IPY 1** and **IPY 2**) for mild steel (MS) in 1.0 M HCl solution. Using weight loss (WL), potentiodynamic polarization (PDP), and electrochemical impedance spectroscopy (EIS), both compounds demonstrated excellent inhibition efficiencies, 96.10% for **IPY 2** and 94.22% for **IPY 2**, at 10^{-3} M and 298 K. The effects of temperature and immersion time were also investigated, revealing stable performance over extended exposure. Thermodynamic analysis showed that both compounds followed the Langmuir adsorption isotherm, with high adsorption equilibrium constants (K_{ads} = 1.39 × 10^5 M^{-1} for **IPY 2** and 1.48 × 10^5 M^{-1} for **IPY 2**) and negative free energy values (ΔG_{ads}° = −39.29 and −39.44 kJ mol^{-1}), indicative of spontaneous, mixed-mode adsorption. Surface characterization *via* Scanning Electron Microscopy (SEM), Atomic Force Microscopy (AFM), FT-IR, UV-visible spectroscopy, and contact angle measurements confirmed the formation of a compact, hydrophobic protective layer on the steel surface. The inhibition mechanism was further elucidated through Density Functional Theory (DFT), Monte Carlo (MC), and Molecular Dynamics (MD) simulations, which supported the strong interaction between the inhibitor molecules and the MS surface. Additionally, *in silico* toxicity assessments revealed low bioaccumulation potential, good biodegradability, and acceptable safety profiles, supporting the environmental compatibility of these compounds. Together, the integration of experimental, theoretical, and toxicological analyses highlights **IPY 1** and **IPY 2** as efficient, stable, and eco-friendly corrosion inhibitors with strong potential for sustainable industrial applications.

Received 21st March 2025
Accepted 13th April 2025

DOI: 10.1039/d5ra02000j

rsc.li/rsc-advances

1 Introduction

Corrosion results from chemical or electrochemical interactions involving metals and alloys and their environment.[1] It represents a widespread concern in many industries and substantially affects profitability and reliability. The impact of corrosion includes major manufacturing interruptions and the need to frequently replace deteriorated components, which results in economic losses and environmental pollution.[2,3] According to the literature, researchers have usually concentrated on studying corrosion, especially in Mild Steel (MS).[4,5] MS garners favor across a diverse range of industrial sectors owing to its attributes, which include commendable strength, cost-effectiveness, and widespread accessibility.[6] However, the composition of mild steel, prominently featuring iron, a notably reactive material, makes it inherently prone to corrosion.[7] This vulnerability is particularly evident in the chemical and petrochemical sectors,[8] where MS directly encounters potent acidic solutions, leading to a shortened operational lifespan and, in some instances, catastrophic failures.[9]

Indeed, there are numerous methods for preventing metal corrosion, including enhancing metal compositions, applying organic and inorganic coatings, and introducing corrosion inhibitors.[10,11] Among these, incorporating corrosion inhibitors appears to be the most beneficial and commonly used approach to protect MS.[12,13] Recent efforts have focused on developing non-toxic inhibitors for acidic environments, particularly for industrial metals such as mild steel.[14] Although plant-based inhibitors have received interest, their variable composition, low solubility, and limited efficiency at high concentrations pose challenges for industrial use.[15] In contrast, synthesized

[a]*Laboratory of Molecular Chemistry, Materials and Environment (LCM2E), Department of Chemistry, Multidisciplinary Faculty of Nador, University Mohamed I, 60700 Nador, Morocco. E-mail: azzouzi.mohamed@ump.ac.ma*

[b]*Department of Mechanical Engineering, Gachon University, Seongnam 13120, Republic of Korea*

[c]*Department of Chemistry, Faculty of Natural and Mathematics Science, University of Prishtina, 10000 Prishtina, Kosovo*

† Electronic supplementary information (ESI) available. See DOI: https://doi.org/10.1039/d5ra02000j

corrosion inhibitors, especially those designed to be non-toxic, offer a more practical and logical alternative, they provide better solubility, stability, and efficiency, making them more suitable for industrial applications.[16] These compounds can be engineered explicitly with functional groups and molecular structures that ensure high solubility and stability in harsh environments, making them highly effective in industrial applications. Additionally, effective corrosion inhibitors typically feature heteroatoms (*e.g.*, oxygen, nitrogen, sulfur), aromatic rings, multiple bonds, and regions of high electron density, enabling strong interactions with metal surfaces.[17,18] Organic compounds can interact physically, chemically, or in a combination way with metal surfaces,[19,20] restricting access to active sites and reducing cathodic, anodic, or both electrochemical processes, resulting in a robust dual-layer protective effect.[21] This mechanism has been extensively explored in previous studies.[22] Physical interactions involve adsorption *via* van der Waals or electrostatic forces, while chemical interactions utilize heteroatoms and conjugated groups to form bonds by donating electrons to the metal surface.[23]

In recent years, several organic compounds have gained prominence in materials science and engineering as corrosion inhibitors.[24,25] These compounds offer a promising avenue to mitigate corrosion by forming protective layers on the metal surface, inhibiting the electrochemical reactions responsible for metal dissolution.[26,27] However, most commercial and synthesized organic inhibitors are toxic, driving the need for more efficient and eco-friendly alternatives. Imidazo[1,2-*a*]pyridine, known for its easy and cost-effective synthesis, is widely regarded as an environmentally friendly building block with a broad spectrum of pharmacological properties. Its distinct structure sets it apart from other organic inhibitors, warranting investigation in corrosion prevention.

The integration of imidazo[1,2-*a*]pyridine heterocycles and Schiff bases within a single molecular scaffold, which are well-established as effective corrosion inhibitors, presents a promising approach for designing highly effective corrosion inhibitors. While imidazopyridine-Schiff base derivatives have been studied for their anticorrosion properties, literature surveys reveal that no investigations have focused on imidazopyrimidine-Schiff base derivatives. Compared to the pyridine ring, the additional nitrogen atom in the pyrimidine ring can significantly alter the compound's electronic properties and reactivity, thereby enhancing corrosion inhibition potential. Heine, the primary objective is to develop two novel imidazo[1,2-*a*]pyrimidine-Schiff base derivatives as corrosion inhibitors that are anticipated to demonstrate a high level of efficacy while ensuring safety and reduced toxicity for both users and the environment. Therefore, (*E*)-2-(4-chlorophenyl)-*N*-(3-nitrobenzylidene)imidazo[1,2-*a*]pyrimidin-3-amine (**IPY 1**) and (*E*)-2-(4-chlorophenyl)-*N*-(2-nitrobenzylidene)imidazo[1,2-*a*]pyrimidin-3-amine (**IPY 2**) were synthesized using an easy, synthetic route allowing scale-up production. **IPY 1** and **IPY 2** were characterized by ^{1}H NMR, ^{13}C NMR, Mass and FT-IR spectroscopic methods. The corrosion inhibition properties in 1.0 M HCl solution at different concentrations, temperatures, and immersion times were studied by methods such as weight loss (WL), potentiodynamic polarization (PDP), and electrochemical impedance spectroscopy (EIS) measurement. In addition, the analysis of the metallic surface was conducted using Scanning Electron Microscopy (SEM), Atomic Force Microscopy (AFM), FT-IR and UV-visible spectroscopic analysis. Furthermore, quantum chemical studies using Density Functional Theory (DFT), Monte Carlo (MC), and Molecular Dynamics (MD) simulations were discussed to provide a better insight into the relationship between the electronic parameters and adsorption mechanism. Additionally, the study includes an *in silico* toxicity assessment, focusing on their human health and environmental profiles.

2 Experimental procedure

2.1. Synthesis

In this study, the imidazopyrimidine-Schiff base derivatives **IPY 1** and **IPY 2** were synthesized according to our earlier publication, using a simple and efficient synthetic approach that adheres to several principles of green chemistry, enabling large-scale production.[28] The structures of the synthesized compounds (Scheme 1) were confirmed by ^{1}H NMR, ^{13}C NMR, FT-IR and mass spectrometry, as detailed in the ESI files (Fig. S1–S10†) lists the assignments for the various chemical shifts of the **IPY 1** and **IPY 2** peaks.

2.2. TGA and DTA analysis

The thermal properties were assessed using Thermogravimetric Analysis (TGA) and Differential Thermal Analysis (DTA) using the DTA PT 1600 instrument. The analyses were performed under standard atmospheric conditions, employing a heating rate of 10 °C min^{-1}, from RT to 600 °C, using alumina (Al_2O_3) crucibles as references.

The TGA (Fig. 1, blue curves) showed that **IPY 1** and **IPY 2** maintained stability up to 281 °C and 246 °C, respectively, with minimal mass loss (~1%) due to absorbed water or residual solvent. The DTA (Fig. 1, red curves) revealed endothermic peaks at around 181 °C and 247 °C for **IPY 2**, corresponding to their melting points. These results indicate that the materials are suitable for applications that require moderate thermal resistance.

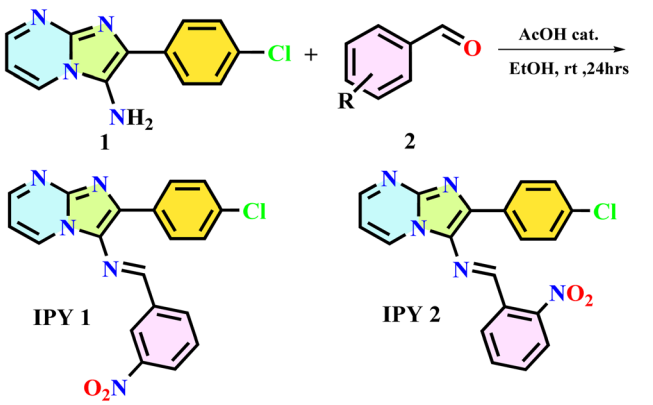

Scheme 1 Synthesis of the new compounds (IPY 1) and (IPY 2).

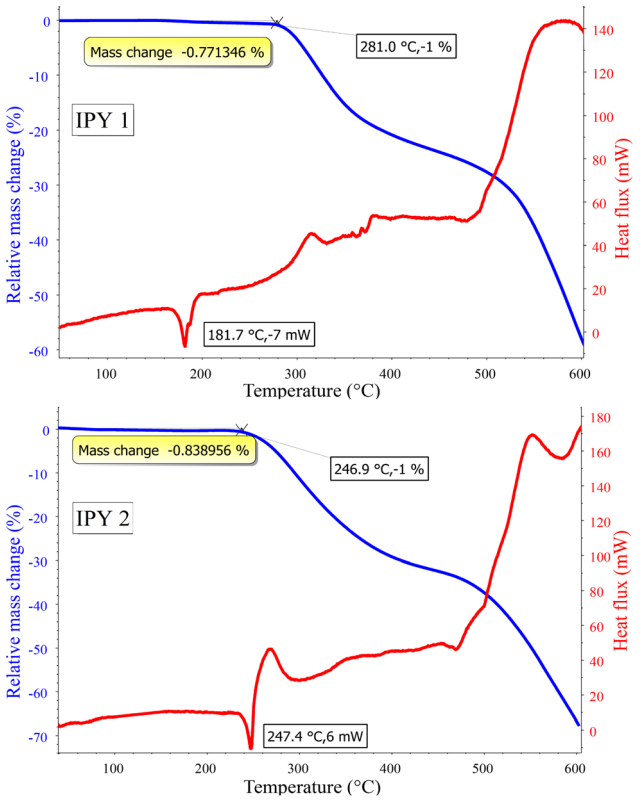

Fig. 1 Thermal analysis of IPY 1 and IPY 2.

2.3. Preparation and cleaning of the MS sample

For all experiments, we used MS samples with a composition of Fe (99.21%), S (0.05%), P (0.09%), Si (0.38%), Al (0.01%), Mn (0.05%), and C (0.21%) by weight. For weight loss studies, the specimens were cut into rectangular shapes with dimensions of $2 \times 2 \times 0.4$ cm, while circular specimens with a uniform surface of 1.0 cm^2 were prepared for electrochemical tests. Before testing, the MS specimens underwent a meticulous preparation process, starting with sequential polishing using abrasive papers graded from 220 to 2000. The samples were cleaned with water, degreased with acetone, and left to air-dry at ambient temperature. To prevent surface oxidation, the samples were promptly utilized in the respective analyses.

2.4. Hydrochloric acid medium

The acidic environment consisted of a 1.0 M HCl solution prepared by diluting analytical-grade 37% HCl from Sigma-Aldrich with bi-distilled water. To carry out different experimental methods, **IPY 1** and **IPY 2** solutions were precisely prepared at distinct concentrations of inhibitors of 1×10^{-3}, 5×10^{-4}, 10^{-4}, 5×10^{-5} and 10^{-5} M within the hydrochloric acid medium. These concentrations were selected based on preliminary screening results, which indicated that inhibition efficiency plateaued near 10^{-3} M, suggesting surface saturation. Moreover, this range is widely used in corrosion studies, allowing for effective comparison with literature reports and ensuring a practical balance between performance, solubility, and environmental relevance.

2.5. Weight loss (WL) measurements

The MS samples were initially weighed with precision and the immersion process was carried out with varying concentrations of IPYs, under controlled conditions at 298 K for a duration of 6 hours. Upon the required time, the MS specimens were carefully retrieved from the test solutions and underwent a thorough cleaning process involving a non-metallic bristle brush, followed by rinsing with distilled water and acetone. Subsequently, the specimens were dried and reweighed with utmost precision using a balance designed for accuracy.[29]

Each experiment was conducted three time to ensure reproducibility. The corrosion parameters such as corrosion reaction rate (CR), surface coverage (θ), and corrosion inhibition efficiency (η%) were calculated by using the corresponding equations.[30,31]

$$C_R = \frac{m_i - m_f}{S \times \Delta t} \quad (1)$$

$$\eta_{WL}\ (\%) = \frac{C_R - C_{R\times inh}}{C_R} \times 100 \quad (2)$$

$$\theta = 1 - \frac{C_{R\times inh}}{C_R} \quad (3)$$

where m_i and m_f represent the mass in mg of the MS coupons before and after immersion, respectively, S denotes the total surface area in cm^2 of the MS coupon, and Δt signifies the immersion time in hours.

2.6. Electrochemical analysis

Electrochemical investigation stands out as a superior approach compared to WL analysis when delving into corrosion behavior. Its primary advantage lies in its ability to swiftly assess the corrosion rate of samples without the need for protracted testing periods. Consequently, this methodology has gained widespread acclaim in the realm of corrosion inhibitor studies.

The experiments used a three-electrode cell configuration, with a platinum counter electrode, a saturated calomel electrode (SCE) as the reference, and a cylindrical mild steel working electrode (WE) characterized by a 1 cm^2 exposed surface area. The pretreatment procedure for the WE mirrored the previously outlined process. Before initiating each experiment, we allowed for a stabilization period lasting 1800 seconds, a duration verified sufficient for achieving a steady-state E_{OCP}. To ensure accuracy, the temperature was controlled in a thermostatic water bath.[32]

PDP measurements were performed in a voltage range of −800 to −200 mV *vs.* SCE, at a scan rate of 0.5 mV s^{-1}. These measurements enabled the extraction of corrosion parameters such as the corrosion potential (E_{corr}) and corrosion current density (i_{corr}) through Tafel extrapolation of the polarization curves. The value of i_{corr} was used to determine the inhibition efficiency η_{PDP} (%) as indicated by eqn (4).[33]

$$\eta_{PDP}\ (\%) = \frac{i_{corr} - i_{corr\times inh}}{i_{corr}} \times 100 \quad (4)$$

where i_{corr} and $i_{corr.inh}$ correspond to the corrosion current densities in the absence and presence of inhibitor, respectively.

Our exploration of corrosion phenomena extended to EIS, encompassing a wide frequency range from 100 kHz to 10 mHz with a perturbation amplitude of 10 mV. The EIS parameters were analyzed using a suitable equivalent circuit to calculate inhibition efficiency η_{EIS} (%), as elucidated in the subsequent eqn (5).[33]

$$\eta_{EIS}\ (\%) = \frac{R_{ct} - R_{ct\times inh}}{R_{ct}} \times 100 \quad (5)$$

where, R_{ct} and $R_{ct.inh}$ signify the charge-transfer resistance in the absence and presence of the inhibitor, respectively.

2.7. UV-vis and FT-IR spectroscopy

This study utilized UV-visible spectrometry to assess the corrosive medium prior to and after immersion of the MS in the medium. For FT-IR, the MS samples were exposed to a 10^{-3} M solution of IPYs for 24 hours, and the MS surface spectra were recorded both before and after immersion.

2.8. Surface morphology analysis

The surface morphology and roughness of the MS specimens were analyzed to investigate morphological changes before and after applying IPYs inhibitors at the optimal concentration, confirming the adsorption process. This analysis was conducted after 24 hours of immersion in aggressive solutions at 289 K. Following immersion, each specimen was rinsed and dried. The SEM observations were conducted using an FEI Nova Nano FEG-SEM 450 microscope, while AFM observations were carried out with a Veeco diInnova atomic force microscope.

2.9. Computational study

DFT and other quantum chemical methods are widely employed to analyse molecular properties, elucidate action mechanisms, and predict inhibitor effectiveness.[34] In this investigation, the molecular geometries of IPY1 and IPY2 were optimized using Gaussian 16 software with the DFT approach.[35] All relevant quantum chemical parameters, including Energy of the Highest Occupied Molecular Orbital (E_{HOMO}), Energy of the Lowest Unoccupied Molecular Orbital (E_{LUMO}), energy gap (ΔE), electronegativity (χ), global hardness (η), softness (σ), fraction of electron transfer (ΔN), and back-donation energy ($\Delta E_{back\text{-}donation}$), were calculated using the following standard equations.[36]

$$\Delta E_{gap} = E_{LUMO} - E_{HOMO} \quad (6)$$

$$I = -E_{HOMO} \quad (7)$$

$$A = -E_{LUMO} \quad (8)$$

$$\chi = \frac{-(E_{HOMO} + E_{LUMO})}{2} \quad (9)$$

$$\eta = \frac{E_{LUMO} - E_{HOMO}}{2} \quad (10)$$

$$\sigma = \frac{1}{\eta} \quad (11)$$

$$\Delta N = \frac{\chi_{Fe} - \chi_{Inh}}{2(\eta_{Fe} + \eta_{Inh})} \quad (12)$$

$$\Delta E_{Back\text{-}donation} = -\frac{\eta}{4} \quad (13)$$

The MC simulation is frequently used to examine how a molecule inhibitor interacts with a metal surface.[37] The adsorption locator, the Forcite module, and the MC simulation approach are all used in Material Studio's MD simulations. In order to find configurations with the lowest conformational energy, this method is mainly utilized to investigate the interactions among inhibitor molecules along with clean steel surfaces under corrosive conditions. All investigated molecular structures are optimized with the COMPASS III force field. The simulation features are derived from previous simulation phases, which used the Fe (110) crystal surface within a simulation box (42.823752 Å × 42.823752 Å × 53.241658 Å). The interface part is modeled with periodic boundary conditions, which eliminate arbitrary border effects. A 40-vacuum layer is also applied to the surface to accommodate the inhibitor and the simulated corrosion medium, which contains 730 water molecules as well as 08 hydronium and 08 chloride ions.

2.10. *In silico* toxicity assessment

The toxicity profiles of IPYs were predicted using two *in silico* tools: ProTox-III[38] and Deep-Pk.[39] Human health-related toxicity was assessed using the ProTox-III server, which employs machine learning algorithms trained on extensive toxicological datasets. Predictions included the median lethal dose (LD_{50}), classified into six toxicity classes (1 = highly toxic to 6 = non-toxic), organ-specific, and toxicity end points. Additionally, pathway targets and Tox21 pathways were analyzed to identify potential biological effects. Environmental toxicity was evaluated using the Deep-Pk tool, a deep-learning-based platform utilizing ecotoxicological data. Endpoints included avian toxicity, biodegradability (based on biological oxygen demand), aquatic toxicity (crustaceans and Daphnia magna), and the bioconcentration factor (BCF).

3 Results and discussion

3.1. WL measurements

Weight loss analysis was employed as one of the simple and reliable methods for evaluating the performance of the inhibitors. The experiments involved immersing MS specimens in a molar HCl medium with varying concentrations of the synthesized IPYs for 6 hours at 298 K. The results summarized in Table 1 include C_R, η_{WL}, and θ values for both IPY1 and IPY2. The findings demonstrate a clear correlation between inhibitor concentration and performance. As the concentrations

Table 1 The corrosion parameters obtained by weight-loss analysis for IPYs

Sample	C (M)	C_R (mg cm^{-2} h^{-1})	η_{WL} (%)	θ
Blank	1	0.972 ± 0.081	—	—
IPY 1	10^{-3}	0.047 ± 0.006	95.16	0.951
	5×10^{-4}	0.065 ± 0.001	93.31	0.933
	10^{-4}	0.079 ± 0.005	91.87	0.918
	5×10^{-5}	0.106 ± 0. 013	89.09	0.890
	10^{-5}	0.138 ± 0.009	85.80	0.858
IPY 2	10^{-3}	0.055 ± 0.002	94.34	0.943
	5×10^{-4}	0.071 ± 0.007	92.69	0.926
	10^{-4}	0.083 ± 0.004	91.46	0.914
	5×10^{-5}	0.120 ± 0.001	87.65	0.876
	10^{-5}	0.146 ± 0.022	84.97	0.849

increase, the corrosion rate of MS significantly decreases. In contrast, the corrosion efficiencies increase reaching 95.16% for IPY1 and 94.34% for IPY2 at 10^{-3} M. These results align with the common trend in corrosion studies, where higher inhibitor concentrations correspond to improved inhibition efficiencies. The enhancement in efficiency with increasing inhibitor levels indicates that IPY1 and IPY2 effectively adsorb onto the MS surface, forming a protective layer.[32] This protective effect becomes more pronounced at higher concentrations, which can be attributed to the adsorption of the studied compounds on the steel surface, providing good metal surface coverage.[40] The following sections will delve deeper into the performance and mechanisms of these inhibitors.

3.2. PDP measurements

This part aims to comprehend the influence of IPYs derivatives at various concentrations on the corrosion kinetics and the dynamics of metal dissolution. Fig. 2 illustrates the PDP curves recorded at 293 K, while Table 2 summarizes the electrochemical parameters, derived from curve extrapolation.

Even at low concentrations, the addition of **IPY 1** and **IPY 2** caused both anodic and cathodic branches to shift towards lower current densities. Therefore, The E_{corr} has just a slight shift within ±30 mV, as seen in Fig. 2 and Table 2, which suggest that IPYs act as a mixed type inhibitor, simultaneously retarding anodic and cathodic processes.[41] A noticeable reduction in i_{corr} was observed as **IPY 1** and **IPY 2** concentration increased. Resulting in a significant increase in inhibition efficiency, reaching 96.10% and 94.22% at 10^{-3} M for **IPY 1** and **IPY 2**, respectively.

Furthermore, the cathodic Tafel branch slopes remained nearly unchanged following the addition of inhibitors, revealing that IPYs do not affect the hydrogen evolution mechanism.[42] In an acidic HCl solution, nitrogen-containing IPYs are protonated into cationic species that outcompete H^+

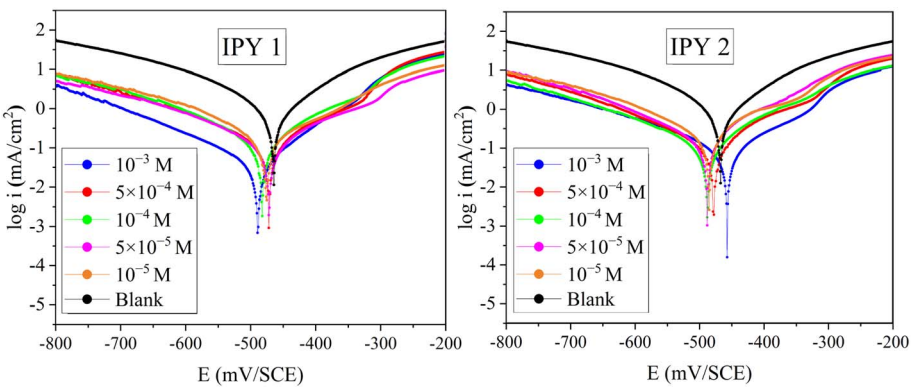

Fig. 2 Tafel curves at various concentrations of IPYs.

Table 2 Tafel polarization parameters for MS in HCl solutions with and without the addition of various concentrations of IPYs

Sample	C (M)	$-\beta_c$ (mV dec^{-1})	β_a (mV dec^{-1})	E_{corr} (mV per SCE)	i_{corr} (mA cm^{-2})	η_{PDP} (%)
Blank	1	163.2	140.4	−467.256	1.328671	—
IPY 1	10^{-3}	157.4	98.0	−491.594	0.051773	96.103
	5×10^{-4}	142.0	97.8	−473.724	0.104034	92.170
	10^{-4}	132.7	113.7	−485.279	0.143260	89.217
	5×10^{-5}	170.4	142.7	−474.596	0.156154	88.247
	10^{-5}	148.0	133.2	−477.496	0.196167	85.235
IPY 2	10^{-3}	164.7	106.1	−456.035	0.076751	94.223
	5×10^{-4}	153.7	117.6	−475.649	0.124015	90.666
	10^{-4}	182.0	132.0	−487.159	0.138847	89.549
	5×10^{-5}	167.9	121.0	−487.527	0.200083	84.941
	10^{-5}	158.5	130.8	−484.734	0.245604	81.515

ions for adsorption sites, effectively covering the steel surface and lowering corrosion activity.[18]

However, the effect of IPYs on the metal dissolution reaction within the anodic branch depends on the applied potential. Initially, the presence of inhibitors leads to a gradual reduction in the iron dissolution rate within the range of E_{corr} and −300 mV per SCE. As the potential increases further, the corrosion rate sharply rises, resembling that of the uninhibited solution. This behavior suggests that the adsorption of IPYs on the metal surface results in forming an organic compact film,[8] providing adequate protection to the steel at lower anodic overpotentials. Nevertheless, the inhibitory efficiency of this protective film diminishes as the potential reaches higher anodic regions.[43] These observations confirm that IPYs effectively adhere onto the steel surface, suppressing hydrogen evolution and retarding anodic dissolution.[44,45]

3.3. EIS measurements

EIS serves as a robust method for exploring metal-electrolyte interactions, including corrosion mechanisms and charge transfer reactions. Fig. 3 presents the Nyquist and Bode plots depicting the behavior of MS, with and without the addition of **IPY 1** and **IPY 2** at 289 K, revealing a single-time constant indicative of charge-transfer control that limits electrochemical kinetics.[46] The depressed semicircles in these plots, caused by the "dispersion effect" due to inhibitor or corrosion particle adsorption on the rough electrode surface, maintain their shape regardless of the inhibitor's presence, suggesting no alteration in the underlying corrosion mechanism.[47] IPY molecules modify the impedance response, increasing capacitance arc diameter and impedance with higher concentrations. Elevated

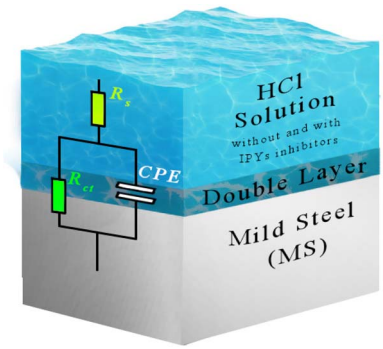

Fig. 4 Equivalent circuit employed to model the EIS results.

phase angles and greater low-frequency impedance confirm IPYs adsorption, forming a protective layer and enhancing corrosion inhibition.[48]

Fig. 4 illustrates the equivalent circuit model applied to simulate the EIS data, incorporating a constant phase element (CPE) to account for the non-ideal semicircles in the Nyquist plots. Replacing the double-layer capacitance (C_{dl}) with CPE improves the analytical precision, offering deeper insights into electrochemical interactions at the metal-electrolyte interface.[49]

Analysis of EIS data yields various corrosion parameters (Table 3), including R_s, R_{ct}, CPE, C_{dl}, phase shift (n), and η_{EIS}. The stability of the corrosive environment, as evidenced by the nearly constant R_s, remains unaltered upon the addition of the inhibitors. However, R_{ct} increases, and C_{dl} decreases with higher **IPY 1** and **IPY 2** concentrations, affirming enhanced corrosion resistance. This suggests effective adsorption of IPYs, displacing water and constructing a compact protective film,

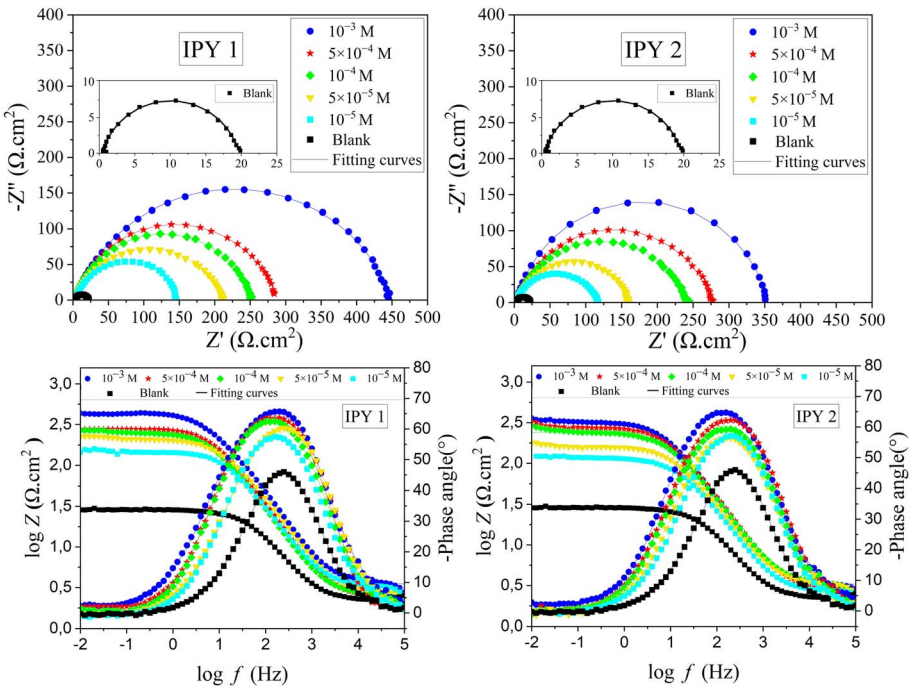

Fig. 3 Nyquist and Bode plots with varying amounts of IPYs.

Table 3 EIS issued data of MS corrosion in molar HCl with and without various amounts of IPYs ($\chi^2 \leq 10^{-3}$)

				CPE			
Sample	C (M)	R_s (Ω cm^{-2})	R_{ct} (Ω cm^{-2})	Q (mF S^{n-1})	n	C_{dl} (μF cm^{-2})	η_{EIS} (%)
Blank	1	1.082 ± 0.079	19.793 ± 0.426	0.950 ± 121.146 × 10^{-6}	0.832 ± 0.024	427.4	—
IPY 1	10^{-3}	3.391 ± 0.127	433.534 ± 4.874	0.096 ± 2.232 × 10^{-6}	0.809 ± 0.003	44.91	95.434
	5×10^{-4}	2.342 ± 0.137	283.505 ± 2.478	0.124 ± 5.586 × 10^{-6}	0.811 ± 0.006	56.29	93.018
	10^{-4}	2.474 ± 0.057	248.401 ± 1.104	0.130 ± 3.986 × 10^{-6}	0.824 ± 0.004	62.46	92.031
	5×10^{-5}	2.639 ± 0.122	204.786 ± 1.196	0.158 ± 7.068 × 10^{-6}	0.815 ± 0.006	72.03	90.334
	10^{-5}	3.079 ± 0.129	145.451 ± 1.068	0.183 ± 9.871 × 10^{-6}	0.818 ± 0.007	81.69	86.391
IPY 2	10^{-3}	2.998 ± 0.057	351.789 ± 1.194	0.121 ± 3.207 × 10^{-6}	0.806 ± 0.003	56.51	94.373
	5×10^{-4}	2.810 ± 0.104	272.238 ± 1.571	0.146 ± 6.842 × 10^{-6}	0.812 ± 0.007	69.05	92.729
	10^{-4}	3.027 ± 0.152	236.819 ± 1.615	0.157 ± 6.572 × 10^{-6}	0.810 ± 0.007	72.82	91.642
	5×10^{-5}	3.064 ± 0.110	157.597 ± 0.957	0.166 ± 6.249 × 10^{-6}	0.825 ± 0.005	76.29	87.440
	10^{-5}	2.610 ± 0.130	112.881 ± 0.744	0.187 ± 3.164 × 10^{-6}	0.829 ± 0.003	84.96	82.465

resulting in decreased MS dissolution rates and increased η_{EIS}, with maximum efficiencies of 95.43% for **IPY 1** and 94.37% for **IPY 2** at 10^{-3} M. Slightly lower n values could be attributed to the adsorption of inhibitor molecules or the formation of metal–IPY complexes.[50]

The decreasing trend in C_{dl} can be explained using the Helmholtz model:[51]

$$C_{dl} = \frac{\varepsilon\varepsilon_0}{d} S$$

The inhibitors reduce the exposed metal surface by adsorbing at the metal–solution interface. Their larger size and lower dielectric constant enhance the double layer's thickness and reduce its dielectric constant, forming a protective layer that shields MS from corrosion.[52]

3.4. Effect of temperature

Temperature is well known to be a factor capable of changing the inhibitory efficacy of organic inhibitors. Its impact on inhibitor performance at the metal–electrolyte interface has been widely studied due to its importance in corrosion processes.[53,54] To investigate this effect, we used the PDP and EIS methods at temperatures ranging from 298 to 328 K, with and without 10^{-3} M of IPYs.

3.4.1. PDP results. Investigation of temperature impact on performance of the inhibitors is depicted in Fig. 5. Table 4 presents the electrochemical parameters extracted from polarization curves in 1.0 M HCl environments with and without the presence of IPYs at 10^{-3} M at various temperatures. A noticeable rise in i_{corr} with increasing temperatures reflects an acceleration in MS corrosion kinetics, indicating possible changes in the

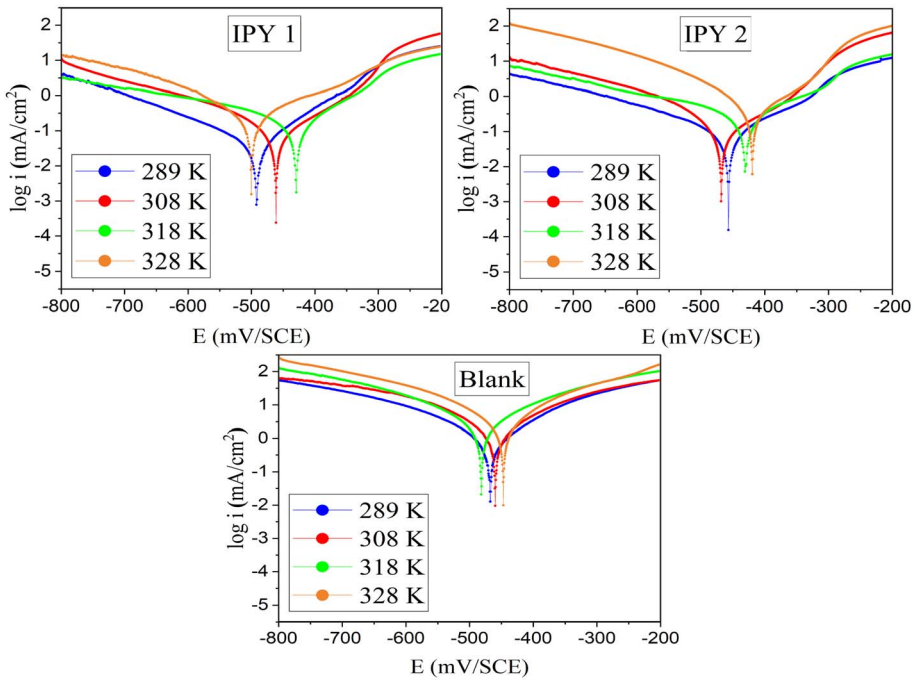

Fig. 5 PDP curves of MS at different temperatures in molar HCl medium at 10^{-3} M IPYs.

Table 4 Polarization findings at different temperatures

Sample	T (K)	$-\beta_c$ (mV dec^{-1})	β_a (mV dec^{-1})	E_{corr} (mV per SCE)	i_{corr} (mA cm^{-2})	η_{PDP} (%)
Blank	298	163.2	140.4	−467.256	1.328671	—
	308	181.6	148.7	−460.078	1.826412	—
	318	174.6	175.3	−481.936	2.417380	—
	328	169.7	156.0	−446.679	3.572790	—
IPY 1 $\times 10^{-3}$	298	157.4	98.0	−491.594	0.051773	96.103
	308	138.0	126.2	−462.074	0.112673	93.830
	318	219.9	104.2	−429.282	0.176141	92.713
	328	169.0	213.9	−499.869	0.425032	88.103
IPY 2 $\times 10^{-3}$	298	164.7	106.1	−456.035	0.076751	94.223
	308	113.8	136.3	−467.964	0.134310	92.646
	318	207.3	115.2	−430.298	0.243423	89.930
	328	119.1	116.6	−419.376	0.530531	85.150

inhibitor–metal interaction. Inhibition efficiency decreases as temperatures increase, dropping from 96.10% to 88.10% for **IPY 1** and from 94.22% to 85.15% for **IPY 2** between 298 and 328 K.

Typically, increasing temperatures weaken the stability of orfgdganic layers or complexes on metal surfaces, leading to their dissociation. This effect reduces the corrosion resistance of MS under elevated temperature conditions.[55]

3.4.2. EIS results. Fig. 6 shows Nyquist plots representing the electrochemical behavior of MS at varying temperatures, both in the absence and presence of 10^{-3} M IPY inhibitors. The plots feature a single capacitive loop, indicating charge transfer control at the MS-solution interface. With increasing temperature, the size of these loops progressively diminishes. Table 5 provides a summary of the corresponding EIS parameters.

Examining Fig. 6 and Table 5 suggests that increasing temperature leads to a marked decrease in R_{ct}, likely due to the disruption of the inhibiting layer. Simultaneously, C_{dl} increases, indicating inhibitor desorption. Despite this, the inhibition efficiency decreases from 95.43% at 298 K to 85.18% at 328 K for **IPY 1**, and from 94.37% at 298 K to 83.23% at 328 K for **IPY 2**. These results indicate that **IPY 1** demonstrates better stability and stronger adsorption on the MS surface compared to **IPY 2**.[56]

3.5. Effect of immersion time

Electrochemical impedance spectroscopy EIS was used to evaluate the effect of immersion time on the corrosion inhibition performance of **IPY 1** and **IPY 2**. This technique was selected for its *in situ* and non-destructive nature, which enables repeated measurements on the same sample over time. Such capability makes EIS especially valuable for monitoring the evolution of electrochemical behavior at the metal–electrolyte interface. In

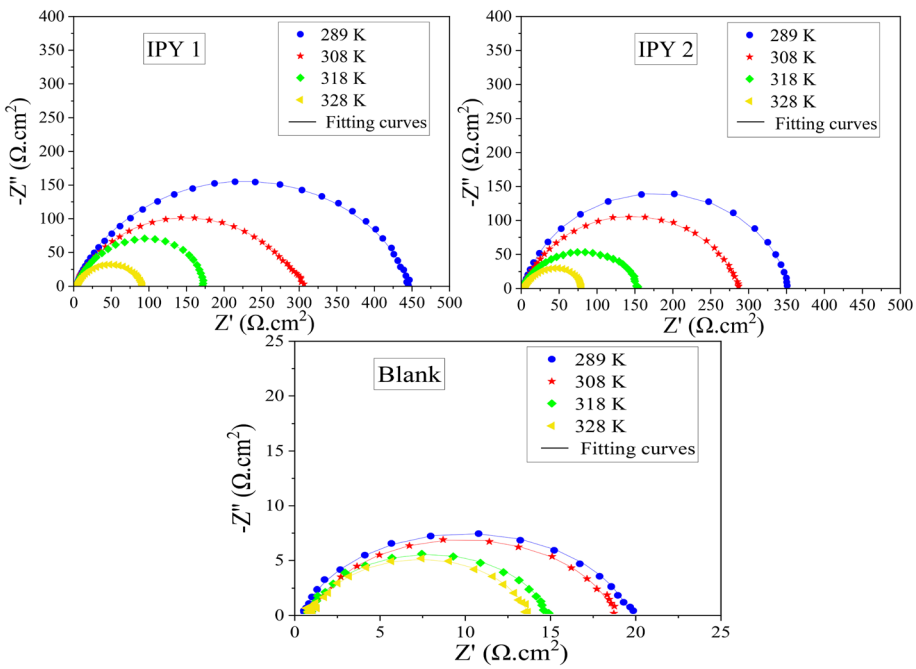

Fig. 6 Nyquist diagrams for (MS, IPYs, 1.0 M HCl) electrochemical system at various temperatures.

Table 5 EIS parameters for (MS, IPYs, 1.0 M HCl) electrochemical system at various temperatures($\chi^2 \leq 10^{-3}$)

Sample	T (K)	R_s (Ω cm^{-2})	R_{ct} (Ω cm^{-2})	CPE		C_{dl} (μF cm^{-2})	η_{EIS} (%)
				Q (mF S^{n-1})	n		
Blank	298	1.082 ± 0.079	19.793 ± 0.426	0.950 ± 121.146 × 10^{-6}	0.832 ± 0.024	427.4	—
	308	1.303 ± 0.056	17.631 ± 0.166	0.897 ± 59.486 × 10^{-6}	0.845 ± 0.012	419.3	—
	318	1.270 ± 0.018	14.005 ± 0.076	1.001 ± 35.971 × 10^{-6}	0.848 ± 0.006	466.4	—
	328	1.322 ± 0.040	12.89 ± 0.130	1.081 ± 86.116 × 10^{-6}	0.838 ± 0.015	517.4	—
IPY 1 × 10^{-3}	298	3.391 ± 0.127	433.534 ± 4.874	0.096 ± 2.232 × 10^{-6}	0.809 ± 0.003	44.91	95.434
	308	3.801 ± 0.107	316.483 ± 1.638	0.114 ± 38.759 × 10^{-6}	0.819 ± 0.046	55.58	94.429
	318	3.024 ± 0.202	172.505 ± 2.649	0.278 ± 72.379 × 10^{-6}	0.823 ± 0.002	144.9	91.881
	328	2.185 ± 0.527	87.027 ± 2.762	0.554 ± 13.531 × 10^{-6}	0.795 ± 0.004	253.5	85.188
IPY 2 × 10^{-3}	298	2.998 ± 0.057	351.789 ± 1.194	0.121 ± 3.207 × 10^{-6}	0.806 ± 0.003	56.51	94.373
	308	3.794 ± 0.100	282.038 ± 1.949	0.128 ± 3.653 × 10^{-6}	0.810 ± 0.004	58.74	93.748
	318	2.385 ± 0.099	154.724 ± 0.777	0.374 ± 3.243 × 10^{-6}	0.837 ± 0.048	215.2	90.948
	328	3.092 ± 0.085	76.897 ± 0.674	0.601 ± 9.811 × 10^{-6}	0.809 ± 0.004	290.8	83.237

this study, measurements were performed at immersion intervals of 0.5 h, 3 h, 6 h, 24 h, and 48 h, and each measurement was conducted in duplicate to ensure accuracy and reproducibility. The results were consistent across repeats, confirming the reliability of the observed trends.

A concentration of 10^{-3} M was chosen for both inhibitors, as it provided the highest efficiency in earlier tests. The Nyquist plots in Fig. 7 illustrate the electrochemical behavior of MS in 1 M HCl, both with and without IPYs inhibitors, at different immersion durations. Notably, as the immersion time increases, there is a conspicuous expansion in capacitance arc diameters indicative of the formation and growth of a protective layer. This trend highlights that the adsorption of the inhibitors onto the MS surface is a time-dependent process.

The electrochemical parameters derived from this study, as detailed in Table 6, provide insights into the dynamic changes occurring over different immersion times. For the inhibited solution, R_{ct} values initially increased up to 3 h, peaking at 95.76% η_{EIS} for **IPY 1** and 94.82% for **IPY 2**. However, extending the immersion time from 3 to 48 h resulted in a decline in R_{ct} values. R_{ct} for **IPY 1** decreased from 535.24 to 239.28, with a slight reduction in η_{EIS} from 95.76% to 94.14%. Similarly, R_{ct} for **IPY 2** dropped from 438.04 to 205.74, accompanied by a decrease in η_{EIS} from 94.82% to 93.19%. The observed reduction in C_{dl} values with prolonged immersion indicates enhanced inhibitor adsorption, reinforcing the protective layer and mitigating corrosion.[57,58]

In summary, the observed changes in electrochemical parameters over varying immersion times underscore the temporal evolution of the inhibitory process. The initial formation and growth of the protective layer contribute to high inhibitory efficiencies, while extended immersion times may lead to the removal of some adsorbed inhibitors and alterations in the protective film. Such behavior aligns well with previously

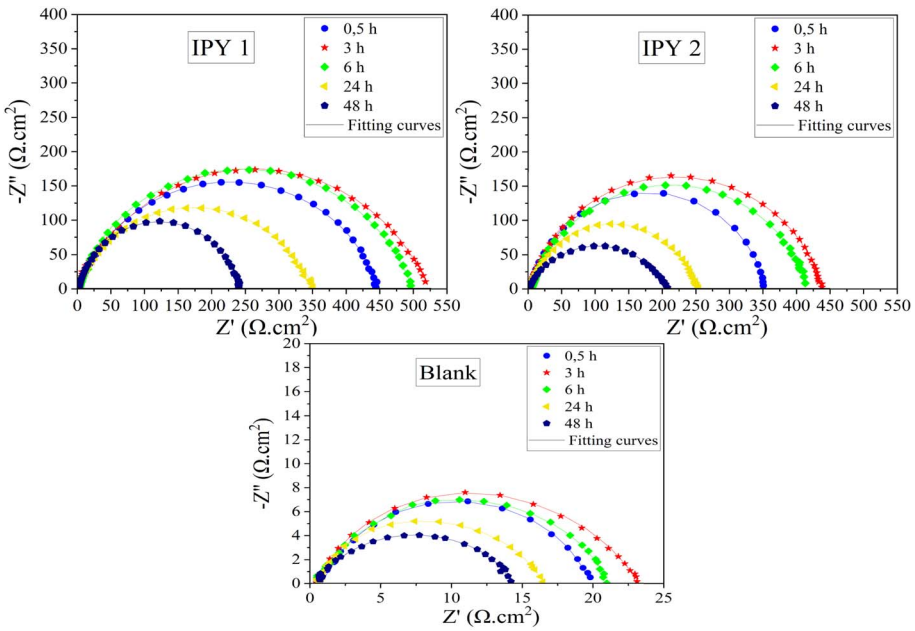

Fig. 7 Nyquist diagrams for (MS, IPYs, 1.0 M HCl) electrochemical system at different immersion times.

Table 6 EIS parameters for (MS, IPYs, 1.0 M HCl) electrochemical system at different immersion times ($\chi^2 \leq 10^{-3}$)

				CPE			
Sample	Time (h)	R_s (Ω cm^{-2})	R_{ct} (Ω cm^{-2})	Q (mF S^{n-1})	n	C_{dl} (μF cm^{-2})	η_{EIS} (%)
Blank	0.5	1.082 ± 0.079	19.793 ± 0.426	0.950 ± 121.1 × 10^{-6}	0.832 ± 0.024	427.4	—
	3	1.025 ± 0.028	22.647 ± 0.115	0.844 ± 82.47 × 10^{-6}	0.855 ± 0.024	431.6	—
	6	1.138 ± 0.057	21.459 ± 0.310	0.908 ± 98.02 × 10^{-6}	0.842 ± 0.013	433.3	—
	24	1.298 ± 0.094	15.834 ± 0.390	1.137 ± 16.16 × 10^{-6}	0.829 ± 0.022	496.4	—
	48	1.290 ± 0.084	13.999 ± 0.258	1.185 ± 51.80 × 10^{-6}	0.825 ± 0.098	496.7	—
IPY 1 × 10^{-3}	0.5	3.391 ± 0.127	433.534 ± 4.874	0.096 ± 2.232 × 10^{-6}	0.809 ± 0.003	44.91	95.434
	3	2.098 ± 0.356	535.241 ± 1.351	0.081 ± 2.203 × 10^{-6}	0.807 ± 0.002	38.24	95.768
	6	2.910 ± 0.035	497.335 ± 2. 03	0.084 ± 1.126 × 10^{-6}	0.792 ± 0.001	36.48	95.685
	24	3.142 ± 0.053	358.637 ± 2.815	0.087 ± 5.479 × 10^{-6}	0.816 ± 0.003	39.80	95.584
	48	2.874 ± 0.043	239.286 ± 2.103	0.092 ± 5.093 × 10^{-6}	0.825 ± 0.002	40.94	94.149
IPY 2 × 10^{-3}	0.5	2.998 ± 0.057	351.789 ± 1.194	0.121 ± 3.207 × 10^{-6}	0.806 ± 0.003	56.51	94.373
	3	3.430 ± 0.128	438.040 ± 1.215	0.117 ± 14.60 × 10^{-6}	0.793 ± 0.011	53.36	94.829
	6	3.963 ± 0.171	413.234 ± 3.611	0.115 ± 3.745 × 10^{-6}	0.813 ± 0.002	57.06	94.807
	24	2.474 ± 0.063	248.142 ± 1.385	0.149 ± 27.17 × 10^{-6}	0.802 ± 0.009	66.01	93.618
	48	2.136 ± 0.127	205.747 ± 2.329	0.157 ± 22.35 × 10^{-6}	0.816 ± 0.009	72.40	93.196

reported studies[59,60] and underscores the importance of considering immersion time when evaluating the long-term stability and effectiveness of corrosion inhibitors in acidic media.[61]

3.6. Adsorption and corrosion activation parameters

The adsorption effectiveness of organic inhibitors was analyzed using well-established isotherms. The relationships between θ and C_{inh} based on the assumptions of these isotherms are described by equations.[62,63]

Langmuir:

$$\frac{C_{inh}}{\theta} = \frac{1}{K_{ads}} + C_{inh} \quad (14)$$

Temkin:

$$\theta = \frac{1}{2\alpha}\ln(K_{ads}) - \frac{1}{2\alpha}\ln(C_{inh}) \quad (15)$$

Frumkin:

$$\ln\left(\frac{\theta}{C_{inh}(1-\theta)}\right) = \ln(K_{ads}) + s\mathrm{d}\theta \quad (16)$$

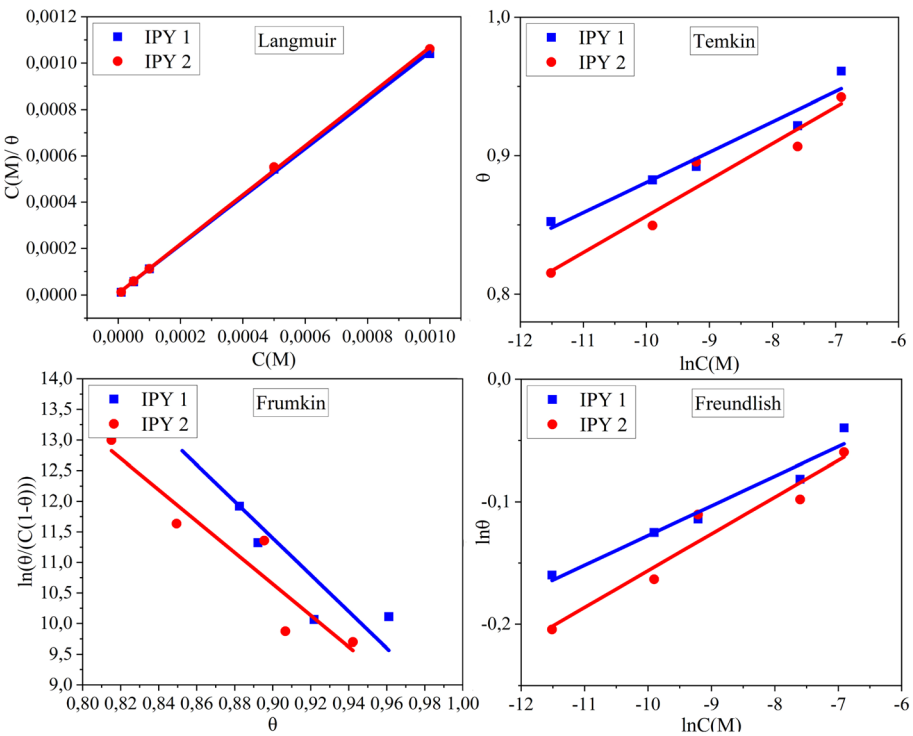

Fig. 8 Four different adsorption isotherms for MS in 1 M HCl containing various concentrations of IPYs at 298 K.

Freundlich:

$$\ln(\theta) = \ln(K_{ads}) + z\ln(C_{inh}) \quad (17)$$

where K_{ads} denotes the equilibrium constant, C_{inh} represents the inhibitor concentration, α signifies the lateral interaction between the inhibitor and the surface, and θ indicates the surface coverage.

The appropriate adsorption isotherm was determined based on data obtained from the PDP method. The isotherm models illustrated in Fig. 8, along with the results presented in Table S12,† demonstrate that the adsorption behavior of IPY inhibitors conforms to the Langmuir isotherm. This conclusion is supported by the high linear correlation coefficients (R^2 = 0.999). This model indicates monolayer adsorption on the surface, leading to the formation of a uniform protective film on the MS.[51]

To derive adsorption equilibrium constant (K_{ads}) and calculate Gibbs free energy of adsorption (ΔG_{ads}°), the intercept of the isotherm plots was employed, using the equation:[64]

$$\Delta G_{ads}^{\circ} = -RT\ln(55.5K_{ads}) \quad (18)$$

Examining the data from the Langmuir adsorption model, the high K_{ads} values suggest the ease with which the two organic compounds adsorb onto the surface. Furthermore, the strongly negative ΔG_{ads}° reflect the spontaneous adsorption of the IPYs. Additionally, ΔG_{ads}° for **IPY 1** and **IPY 2** ($\sim$−40 kJ mol^{-1}) are suggestive of a combination of physisorption and chemisorption, with a predominant contribution from chemisorption. This indicates a charge transfer process between the inhibitors and the metal surface, resulting in the formation of coordination bonds that secure the inhibitors onto the metal in a stable and adhesive manner.[65,66]

To elucidate the adsorption process and ascertain the activation parameters of MS dissolution, the Arrhenius kinetic model was applied to the data obtained from PDP tests conducted over the temperature range of 298→328 K. The Arrhenius equation (eqn (19)) and the transition state (eqn (20)) were employed to construct the model. Plotting the $\ln(i_{corr})$ *vs.* $\frac{1}{T}$ (Fig. 9a) allowed for an estimation of E_a. Furthermore, ΔH_a and ΔS_a of activation were calculated from the $\ln\left(\frac{i_{corr}}{T}\right)$ *vs.* $\frac{1}{T}$ plot, as depicted in Fig. 9b. The derived thermodynamic parameters are summarized in Table S13.† [67]

$$\ln(i_{corr}) = \ln(A) - \frac{E_a}{RT} \quad (19)$$

$$\ln\left(\frac{i_{corr}}{T}\right) = \frac{\Delta S_a}{R} + \ln\left(\frac{R}{N_a h}\right) - \frac{\Delta H_a}{RT} \quad (20)$$

where i_{corr} is the corrosion current density, E_a represents the activation energy, ΔH_a, ΔS_a represents the enthalpy and the entropy of activation, and A denotes the Arrhenius pre-exponential factor. R is the universal gas constant, N_a is Avogadro's number and h is Planck's constant.

The resulting linear fit, which is seen in Fig. 9, exhibit correlation coefficients (R^2) of 0.982 or higher than 0.982, demonstrating that the Arrhenius kinetic model is a suitable fit for determining how temperature affects the rate of corrosion.[68]

The calculated E_a values for inhibited solutions are higher than those for the uninhibited medium, indicating that the presence of **IPY 1** and **IPY 2** reduces the corrosion rate by slowing the MS dissolution process.[69] Additionally, the positive values of ΔH_a confirm that the metal dissolution is endothermic, which explains the decline in inhibition efficiency at elevated temperatures. The higher ΔH_a values for inhibited solutions suggest a slower dissolution in the presence of IPYs. The ΔS_a values provide insight into the system's order–disorder dynamics. Increased ΔS_a values in the inhibited solutions indicate greater disorder during the formation of the activated complex. This heightened entropy is attributed to the adsorption of inhibitors on the MS surface, leading to the displacement of numerous water molecules and Cl^- ions previously adsorbed on the steel surface.[70,71]

3.7. UV-visible and FT-IR analysis

Organic inhibitors have garnered significant attention in recent years, particularly those capable of interacting with metal ions on surfaces, forming insoluble chelates or complexes that improve corrosion resistance. To explore the possible formation of IPY-Fe complexes, which result from interactions with iron

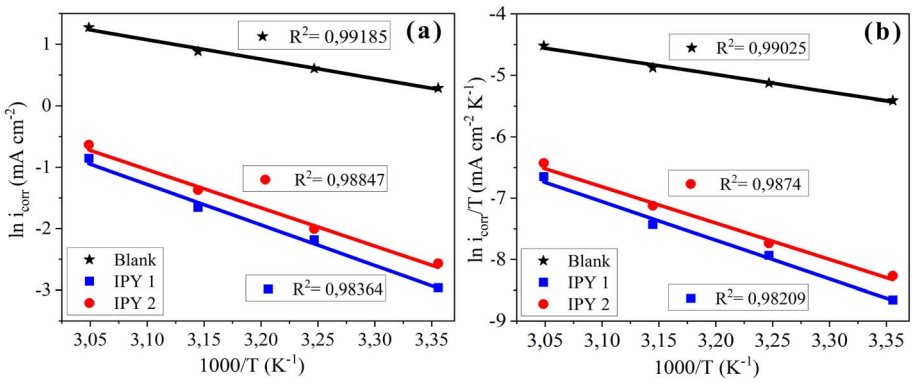

Fig. 9 (a) Arrhenius and (b) transition state plots.

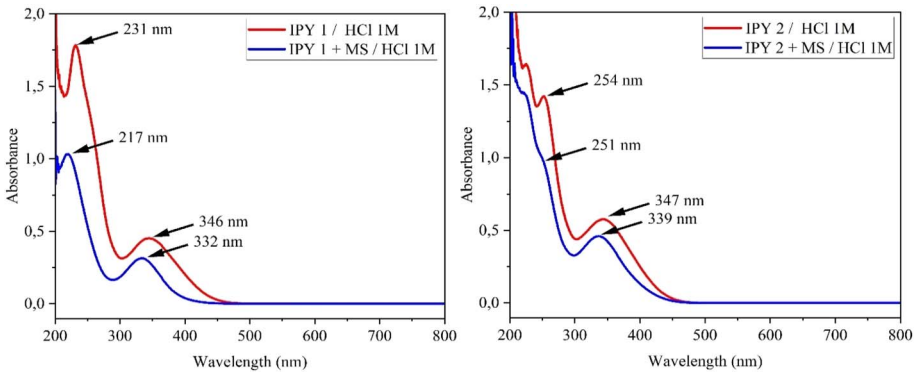

Fig. 10 The recorded UV/Vis spectra before and after immersion of mild steel.

ions generated during the corrosion process, UV-visible spectroscopy was used. Absorption spectra were obtained for solutions containing 10^{-3} M inhibitors, both prior to immersion (depicted as the red curve) and after 7 days of mild steel immersion (shown as the blue curve), as presented in Fig. 10.

Prior to immersing mild steel, distinct peaks and shoulders manifested around 231 nm and 346 nm for **IPY 1** and 254 nm and 347 nm for **IPY 2**. These peaks align with π–π* transitions, engaging the compound's electronic structure. Simultaneously, the shoulders may be associated with n–π* electron transitions involving the lone pair electrons of the heteroatoms within the compound.

After 7 days in the acidic medium, a shift in the absorption maxima (λ_{max}) was observed. The peaks shifted to 217 nm for **IPY 1** and 251 nm for **IPY 2**, while the shoulder maxima for n-π transitions moved to 332 nm for **IPY 1** and 339 nm for **IPY 2**. These changes confirm the inhibitors' interaction with Fe ions through π electron and lone pair coordination with the d-orbitals of Fe atoms, resulting in the formation of chemical bonds. The reduced intensity of the absorption peaks post-immersion further indicates that IPY inhibitors reacted with ferrous ions generated during anodic corrosion, forming stable IPY–Fe complexes on the steel surface.[72,73]

FTIR analysis was conducted to investigate the protective layer formed by IPYs after immersion in a corrosive solution containing 10^{-3} M of IPYs. The FTIR spectra of pure **IPY 1** and **IPY 2** (red line) and those of the metal surface post-immersion (blue line) are illustrated in Fig. 11.

The FTIR analysis of the immersed MS surface revealed peaks corresponding to the functional groups of the inhibitors, confirming the presence of IPYs on the metal surface. While some peaks showed reduced intensity compared to the pure inhibitor spectra, indicating a depletion of molecules, a slight shift towards lower wavenumbers suggested active participation in the adsorption process on the steel surface.[74]

These experimental results strongly indicate that IPYs molecules adsorb onto the MS surface, forming a protective film. This barrier effectively reduces the corrosion rate by limiting reactions at the active sites of the steel.

3.8. Contact angle

The protective action of organic inhibitors against corrosion involves replacing water molecules adsorbed on the metal surface, leading to the formation of a protective inhibitor film. This process often imparts hydrophobic properties to the metal

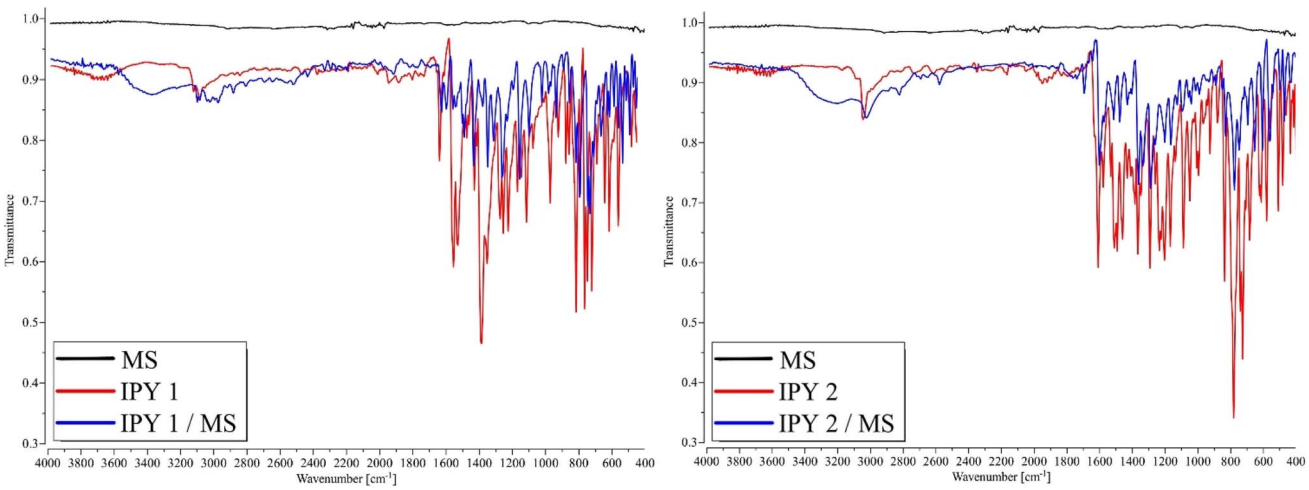

Fig. 11 FTIR-ATR spectra of blank steel, IPYs and steel with inhibitors.

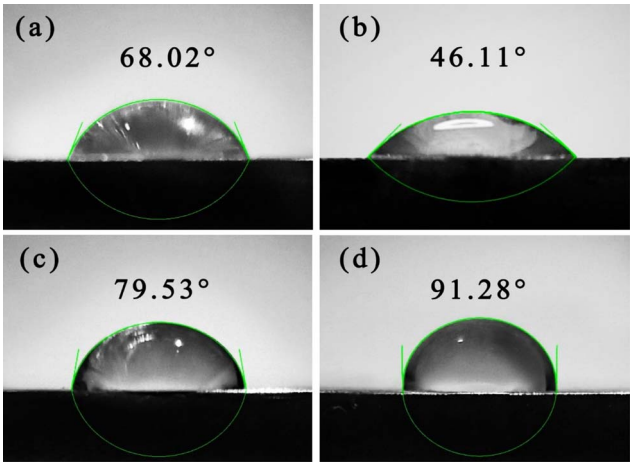

Fig. 12 Contact angles measurements: (a) polished, (b) 6 hours of exposure to molar HCl medium without inhibitors, and with (c) **IPY 1** and (d) **IPY 2**.

surface.[23] To assess the hydrophobic or hydrophilic nature of the MS surface, contact angle were investigated, with the finding represented in Fig. 12. For freshly polished MS, the contact angle was recorded at 68.02°, which decreased to 46.11° after 6 hours in an uninhibited acidic solution. This reduction suggests an increase in surface hydrophilicity, likely resulting from the appearance of polar corrosion-related substances.[75] Conversely, the MS surface treated with 10^{-3} M solutions of IPY inhibitors exhibited increased contact angles: 79.53° for **IPY 1** and 91.28° for **IPY 2**. This rise in contact angle indicates enhanced hydrophobicity, attributed to the presence of IPYs on steel surface. The observed increase in hydrophobicity can be linked to the alignment of hydrophobic groups of IPYs on the MS surface.[76,77] These findings strongly suggest that IPYs effectively adsorb onto the metal surface, forming a hydrophobic protective layer that reduces the interaction between the corrosive medium and the metal. This protective layer highlights the inhibitors' capability to mitigate corrosion.[78,79]

3.9. Surface morphology analysis

To obtain more detailed information about the effect of IPYs on surface changes of MS, SEM and AFM analyses were performed, both with and without **IPY 1** and **IPY 2**. The resulting images, depicted in Fig. 13, compare the well-polished MS samples with those exposed to uninhibited and inhibited acidic solutions for 24 hours at 289 K. As presented in Fig. 13, the polished MS surface displays a smooth and uniform texture with faint scratches caused by sandpaper. However, exposure to the uninhibited acidic solution resulted in significant surface damage, leaving the surface highly irregular and severely corroded due to extensive metal dissolution.

In contrast, the MS surfaces treated with inhibited solutions containing **IPY 1** or **IPY 2** showed minimal surface degradation and a considerably smoother than the uninhibited sample. This improvement is ascribed to the development of a protective inhibitor film on the steel surface, which mitigates the metal

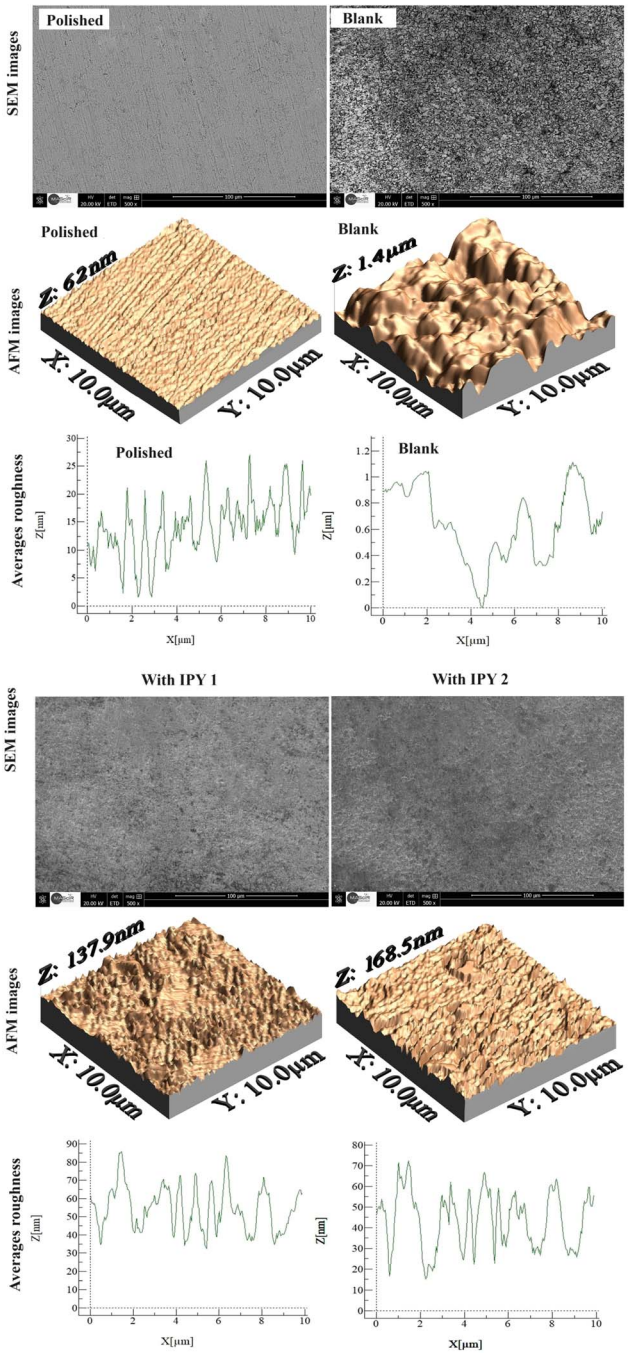

Fig. 13 Visualization of the corrodent and modified mild steel surface by SEM and AFM techniques.

dissolution.[80,81] SEM and AFM analyses indicate a significant reduction in corrosion in the inhibited solutions, aligning with and further validating the conclusions drawn from earlier experimental findings in this study.

3.10. Computational approach

3.10.1. DFT results. The graphical representation in Fig. 14 unveils the HOMO and LUMO orbitals, for the **IPY 1** and **IPY 2** compounds. The HOMO electron densities extensively cover the

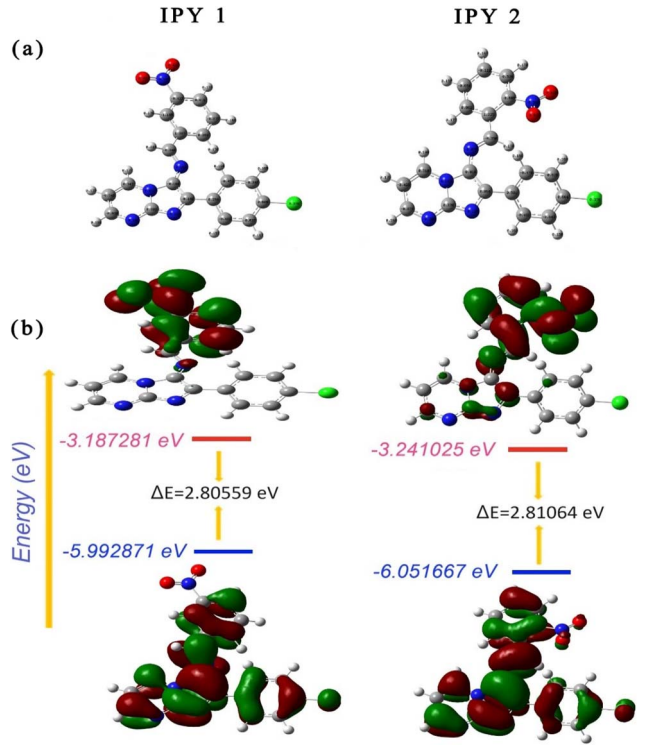

Fig. 14 (a) Optimized structure, (b) HOMO, LUMO of **IPY 1** and **IPY 2** compounds.

structures of both compounds, owing to the high electron density of nitrogen, oxygen, chlorine atoms, and electron-rich aromatic rings. This feature enhances the ability of **IPY 1** and **IPY 2** to donate electrons to vacant metal orbitals. Conversely, the LUMO electron density is concentrated over the imine function and the *meta* and *ortho* positions of the (nitrophenyl), indicating a propensity to receive electrons from the Fe surface. Consequently, **IPY 1** and **IPY 2** demonstrate a dual capacity for both electron donation and acceptance, facilitating donor–acceptor interactions with the metal's valence orbitals.

Quantum chemical parameters presented in Table 7 contribute to evaluating the corrosion inhibition performance. The E_{HOMO} relates to the ability of a molecule to share electrons with the d orbital of the metal surface, and the energy of the lowest unoccupied molecular orbital (E_{LUMO}) represents the ability to accept electrons from the metal. However, compounds with a higher E_{HOMO} are readily adsorbed to the metal surface and provide better inhibitory efficacy.[82,83]

Enhancing the transport process through the adsorbed layer is instrumental in increasing the inhibitor's efficiency since increased values of E_{HOMO} facilitate the inhibitor's adsorption.[84] In the case of **IPY 1** and **IPY 2**, a decrease in E_{HOMO} follows the sequence E_{HOMO} (**IPY 1**) > E_{HOMO} (**IPY 2**), aligning with the experimental inhibitor efficiency results. This suggests that **IPY 1**, with a higher E_{HOMO}, has enhanced adsorption potential on the metal surface, contributing to its inhibitory effectiveness. Moreover, the energy gap (ΔE_{gap}) is a crucial factor in describing the molecular reactivity. A lower ΔE_{gap} value indicates easier electron transfer from the HOMO to the LUMO molecular orbital, which corresponds to higher inhibitory efficiency.

In the studied compounds, IPY1 exhibits a lower ΔE_{gap} (2.80559 eV) compared to IPY2 (2.81064 eV), indicating higher reactivity for **IPY 1**. This aligns with its experimental performance, emphasizing its superior capacity to accept electrons from the iron d-orbital, enhancing stability, and facilitating effective adsorption to the metal surface, increasing the effectiveness of its inhibitory effect.[85]

Chemical hardness (η) and softness (σ) are key properties for evaluating a molecule's stability and reactivity.[86] According to the literature, a soft molecule typically has a small ΔE_{gap}, and high corrosion inhibition efficiency is associated with a low η value and a high σ value. Based on the η and σ parameters of the inhibitors studied, it is evident that the **IPY 1** inhibitor has the lowest η value (1.402795 eV) and the highest σ value (0.712862 eV), which accounts for its superior efficiency compared to **IPY 2**. Furthermore, examining the ΔN (fraction of transferred electrons) and $\Delta E_{back\text{-}donation}$, IPY1 holds a more favorable electron back-donation capacity, as indicated by $\Delta E_{back\text{-}donation}$ value (−0.530698). This aligns with its superior inhibitory effect observed experimentally.

The electrophilic and nucleophilic attack regions of **IPY 1** and **IPY 2** compounds were illustrated in the molecular Electrostatic Surface Potential (ESP) map (Fig. 15), that provides a visual representation of the charge distribution on the molecular surface. In this map, the nucleophilic (red) regions are prominently positioned around oxygen (O) and nitrogen (N) atoms, indicating their potential as covalent bonding centers. These regions are crucial in promoting corrosion inhibition, as they facilitate strong chemical bonds between the inhibitor molecules and the steel surface, thereby preventing the onset of corrosion. The presence of these nucleophilic regions underscores the importance of heteroatoms, in the design of effective corrosion inhibitors.[87,88]

To identify the active regions of the inhibitors studied, Mulliken charges were calculated and are shown in Fig. 16. The charge distribution on the atoms of **IPY 1** and **IPY 2** highlights heteroatoms with negative charges and an excess of electron density, designating them as nucleophilic centers during interaction with the iron surface. As shown in Fig. 16, atoms N, C, and O in both molecules exhibit the most negative charges, designating them as primary contributors to nucleophilic

Table 7 The calculated quantum chemical descriptors for the IPY1 and IPY2 compounds

Theoretical parameters	IPY 1	IPY 2
E_{HOMO} (eV)	−5.992871	−6.051667
E_{LUMO} (eV)	−3.187281	−3.241025
ΔE (E_{HOMO} − E_{LUMO}) (eV)	2.80559	2.81064
I (eV)	5.992871	6.051667
A (eV)	3.187281	3.241025
χ (eV)	4.590076	4.646346
η (eV)	1.402795	1.405321
σ (eV^{-1})	0.712862	0.711581
ΔN	0.081952	0.061784
$\Delta E_{back\text{-}donation}$	−0.530698	−0.531330

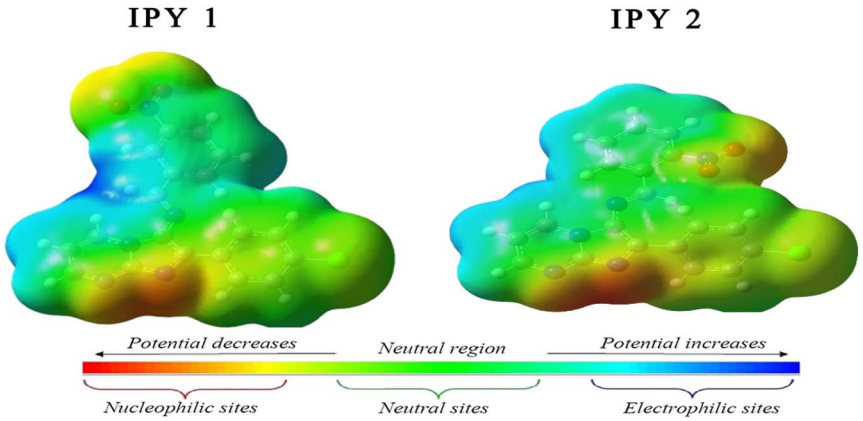

Fig. 15 ESP maps of IPY 1 and IPY 2 compounds.

centers. In their interaction with the iron surface, these atoms will likely play a pivotal role, serving as active adsorption centers.

3.10.2. MD and MC simulations. Understanding the fundamental mechanisms of corrosion inhibition necessitates a theoretical foundation, enabling predictions of geometric

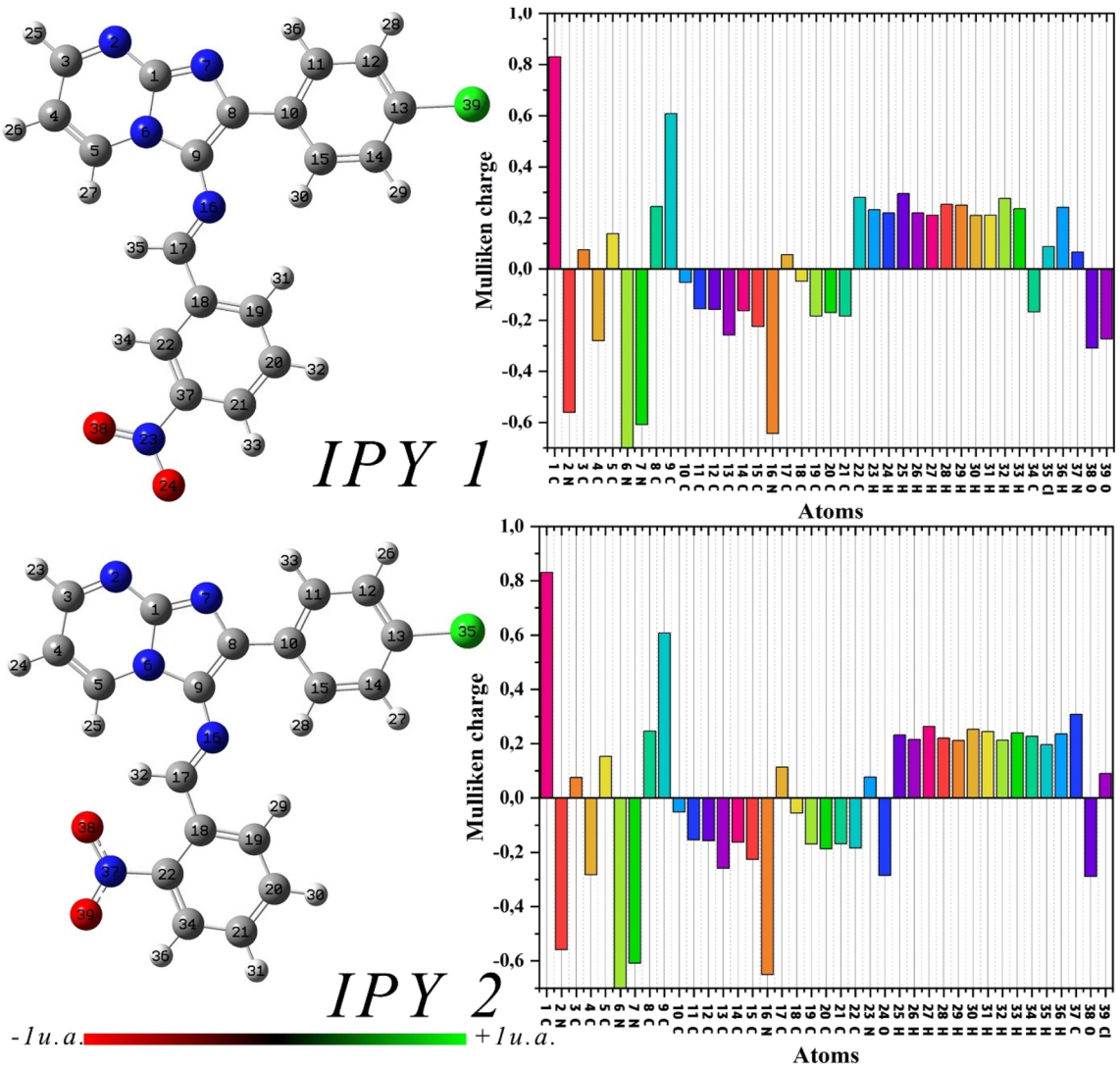

Fig. 16 Mulliken atomic charge distribution for IPY 1 and IPY 2 compounds.

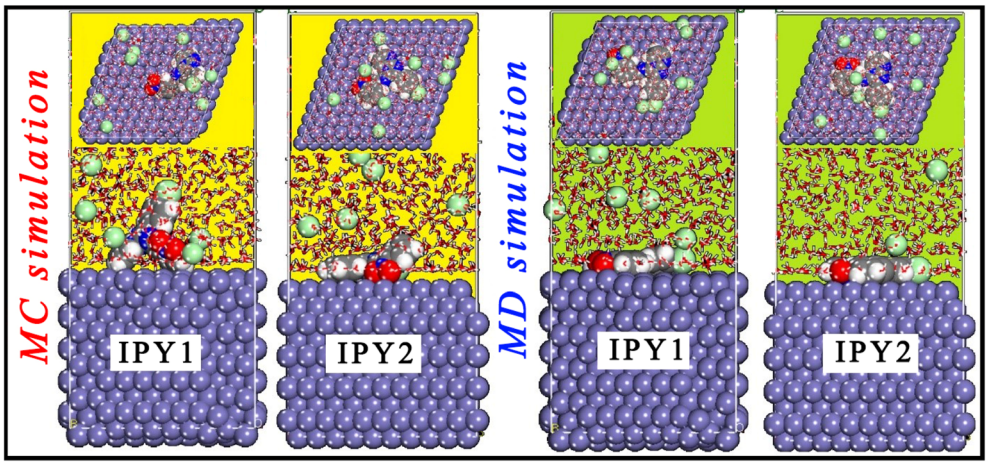

Fig. 17 MC and MD results for IPY 1 and IPY 2 compounds.

structures and adherence patterns of corrosive entities to metal surfaces. Therefore, an exploration of corrosion inhibitor adsorption in corrosive solutions and its inhibition mechanisms becomes crucial.[89] MD is used to simulate a wide variety of systems, from single molecules to materials. It can be used to study dynamic processes such as diffusion, molecular conformation, and chemical reactions, as well as the thermodynamic and structural properties of systems.[90] In MC simulations, the adsorption energy is a key parameter used to characterize the interaction between a compound and a surface. It represents the energy change associated with the adsorption process, where compounds adhere to the surface of a material. Fig. 17 illustrates the lowest energy configuration of **IPY 1** and **IPY 2** compounds on the Fe(110) surface. Both inhibitors are adsorbed onto the Fe(110) surface, adopting a configuration that maximizes surface contact through their nitrogen, oxygen, and chlorine atoms.[91] Fig. 18 presents the adsorption energies (kcal mol^{-1}) of the inhibitors. The data show that **IPY 1** exhibits a more negative adsorption energy ($E_{ads} = -218.85$ kcal mol^{-1}) compared to **IPY 2** ($E_{ads} = -203.75$ kcal mol^{-1}), indicating stronger interaction with the Fe(110) surface. These results suggest that **IPY 1** is likely to be the more effective corrosion inhibitor.[92]

The adsorption on metal surfaces can be assessed through the Radial Distribution Function (RDF) analysis of the MD trajectory derived from corrosion simulations. This technique is fundamental for such investigations.[93]

The RDF analysis is utilized to characterize the adsorption nature of **IPY 1** and **IPY 2** inhibitors on the metal surface. According to existing literature, a peak between 1 and 3.5 Å typically signifies a chemical bond between the inhibitor and the metal surface, while a peak beyond 3.5 Å indicates a physical bond. Fig. 19 illustrates the RDF of the Fe (110) surface in relation to specific atoms of IPY 1 and **IPY 2** inhibitors in this study.

Fig. 19 shows that the RDF value for oxygen atoms in **IPY 1** is 2.95 Å, for nitrogen atoms is 3.31 Å, and for chlorine atoms is 3.19 Å from the Fe(110) surface [125]. In comparison, **IPY 2** absorbs oxygen atoms with an RDF distance of 2.87 Å, nitrogen atoms at 3.15 Å, and chlorine atoms at 3.31 Å. The close proximity of the **IPY 1** and **IPY 2** atoms to the metal surface confirms a strong interaction between the inhibitors and the metallic surface.[94]

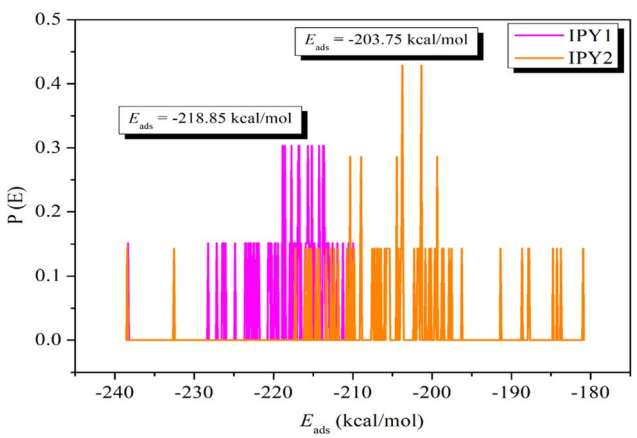

Fig. 18 Distribution of the E_{ads} of IPY 1 and IPY 2 compounds on the Fe(110) surface.

3.11. The inhibition mechanism

Organic compounds containing heteroatoms, and bonds such as C=C and C=N, effectively inhibit corrosion by adsorbing onto metal surfaces *via* lone pair electrons. This adsorption at the steel/solution interface blocks reactive sites and lowers corrosion activation energy, reducing MS corrosion.[95]

In HCl solutions, **IPY 1** and **IPY 2** protonate into cationic species, enhancing interaction with chloride ions and leading to physical adsorption and the formation of a protective $(FeCl–IPY^{+})_{ads}$ layer. Their larger size allows these inhibitors to effectively compete for adsorption sites, covering the steel surface, reducing H^{+} ion interaction with reactive sites, and mitigating corrosion activity.[96]

Furthermore, the lone pair electrons and the π-bonds act as key contributors to the formation of a protective layer. These

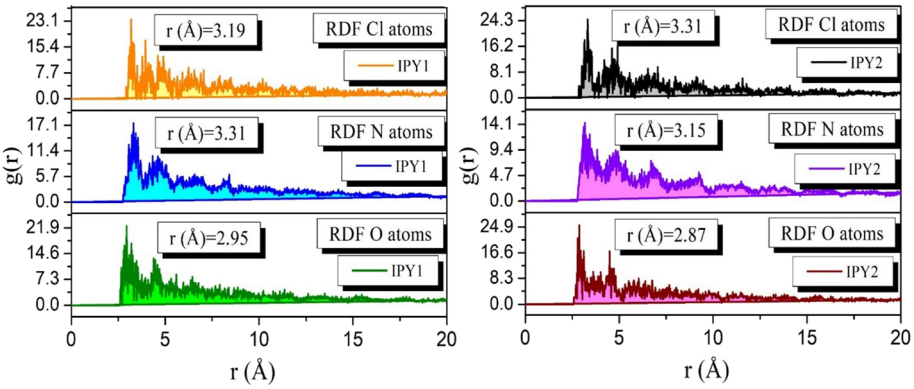

Fig. 19 RDF analysis of IPY 1 and IPY 2 on the Fe surface.

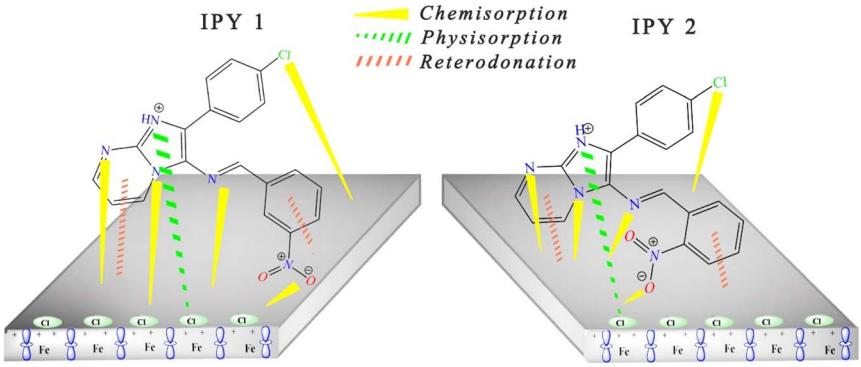

Fig. 20 Adsorption mechanism of IPYs on the MS surface.

serve as multiple adsorption centers in the chemisorption process, interacting with the vacant d-orbitals of iron atoms. Simultaneously, back-bonding (retrodonation) occurs as iron-occupied orbitals supply electrons back to the inhibitor molecules, reinforcing the stability of the adsorption layer.[97]

Fig. 20 depicts the proposed mechanism for the adsorption of IPYs on the MS surface in an acidic medium, illustrating the interplay of physisorption and chemisorption in forming a robust protective film.

4 Comparison of investigated inhibitors with reported related derivatives

The corrosion inhibition efficiencies of the studied inhibitors were evaluated in comparison with closely related derivatives. Table 8 summarizes the performance of various imidazo[1,2-*a*] pyridine derivatives at a concentration 10^{-3} M for MS in molar HCl medium. The analysis highlights that the investigated IPY derivatives exhibit superior corrosion inhibition efficiency relative to their counterparts. This enhanced performance can be attributed to the structural features of the imidazo[1,2-*a*] pyrimidine framework, which incorporates two nitrogen atoms compared to the single nitrogen in the pyridine ring. Additionally, the presence of Cl and NO_2 substituents further enhances the inhibitors' protective capabilities by facilitating adsorption and film formation on the MS surface.

These findings underscore the significant advantages of the studied IPY derivatives in corrosion inhibition, showcasing their potential for advancing corrosion protection strategies.

5 Toxicity assessment

5.1 Toxicity analysis of human health implications

The *in silico* toxicity assessment of **IPY 1** and **IPY 2**, conducted using the ProTox-III server,[49] provided valuable insights into the safety profiles of these compounds, particularly regarding their handling and potential accidental exposure (Table 9). As these molecules are designed for industrial corrosion inhibition applications rather than human consumption, the analysis emphasizes their safety under controlled usage. The analysis incorporated general toxicity,[103] organ toxicity,[38] toxicity endpoints,[104] Tox21 pathways,[105] and molecular pathways.[106] General toxicity predictions classified both molecules in Toxicity Class 3 (out of 6), with a predicted LD_{50} of 1800 mg kg^{-1}. This classification indicates mild toxicity, suggesting moderate risks if exposure occurs under improper conditions. Organ toxicity predictions indicated active hepatotoxicity and neurotoxicity, with probabilities of 0.52 and 0.62, respectively. However, the low probabilities reduce the certainty of these predictions. Nephrotoxicity was predicted as inactive, with

Table 8 Comparative analysis

Inhibitor	IE (%)	Ref.	Inhibitor	IE (%)	Ref.
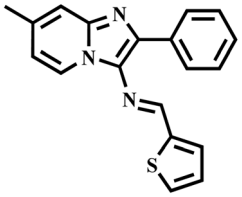	91	98	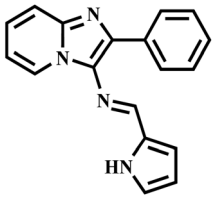	86	99
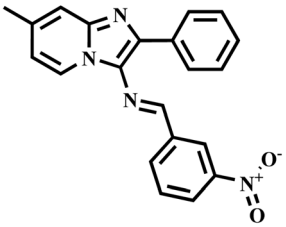	86	100	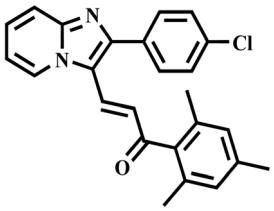	88	101
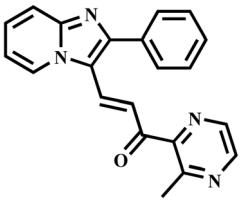	92	102	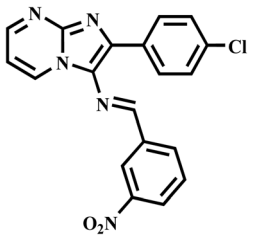	96	This work

a probability of 0.70, indicating a low likelihood of kidney-related toxicity. Respiratory toxicity was predicted as active with a probability of 0.53, reflecting a mild potential for respiratory system effects. Although flagged as active, the low probabilities (<0.7) across these predictions suggest limited risks under controlled conditions. The analysis of toxicity endpoints revealed activity for carcinogenicity, mutagenicity, and immunotoxicity, with probabilities of 0.62, 0.89, and 0.54, respectively. The relatively higher probability of mutagenicity highlights the need for awareness, but the other endpoints suggest only mild potential risks.[107] Cytotoxicity and clinical toxicity were predicted as inactive, with probabilities of 0.63 and 0.53, respectively, indicating minimal concerns in these areas. Tox21 pathway analysis showed limited activity for the aryl hydrocarbon receptor (AhR) and mitochondrial membrane potential (MMP) pathways, with probabilities of 0.50 and 0.55, respectively, suggesting a mild potential for endocrine disruption[108] and mitochondrial effects.[109] In contrast, inactivity was

Table 9 Toxicity assessment results for **IPY 1** and **IPY 2** based on *in silico* predictions

Category	Target	Prediction	Probability
General toxicity	Predicted LD_{50}	1800 mg kg^{-1}	—
	Toxicity class	3 (out of 6)	—
Organ toxicity	Hepatotoxicity	Active	0.52
	Neurotoxicity	Active	0.62
	Nephrotoxicity	Inactive	0.70
	Respiratory toxicity	Active	0.53
Toxicity end points	Carcinogenicity	Active	0.62
	Mutagenicity	Active	0.89
	Cytotoxicity	Inactive	0.63
	Immunotoxicity	Active	0.54
	Clinical toxicity	Inactive	0.53
Tox 21 pathways	Aryl hydrocarbon receptor (AhR)	Active	0.50
	Mitochondrial membrane potential	Active	0.55
	Nuclear factor pathways (Nrf2/ARE)	Inactive	0.74
Molecular pathways	Androgen receptor (AR)	Inactive	0.97
	Estrogen receptor alpha (ERα)	Inactive	0.85

Table 10 Predicted environmental toxicity profiles for IPY 1 and IPY 2

Property name	Predicted value	Property unit	Predictive confidence
Avian	Safe	Category (safe/toxic)	0.014
Bioconcentration factor	0.12	$\log_{10}$ (L kg^{-1})	—
Biodegradation	Safe	Category (safe/toxic)	0.0
Daphnia magna	8.31	$-\log_{10}[(\text{mg L}^{-1})/(1000 \times \text{MW})]$	—
T. Pyriformis	−16.4	$-\log_{10}[(\text{mg L}^{-1})/(1000 \times \text{MW})]$	—

predicted for the Nrf2/ARE pathway (probability 0.74), reflecting minimal oxidative stress concerns. Furthermore, molecular pathway predictions indicated inactivity for both androgen and estrogen receptor pathways, with high probabilities of 0.97 and 0.85, supporting a low likelihood of endocrine system interactions. However, the majority of active predictions were associated with low probabilities, suggesting limited confidence in their potential effects. Given their intended use for industrial applications and the non-consumable nature, **IPY 1** and **IPY 2** exhibit manageable safety profiles, with limited concerns under proper safety protocols.

5.2. Environmental toxicity analysis

The environmental toxicity profiles of **IPY 1** and **IPY 2**, assessed using the Deep-Pk tool, provide encouraging insights into their ecological safety. As summarized in Table 10, the predictions were obtained using the Deep-Pk tool.[39] Both compounds are predicted to be safe for avian species, indicating minimal risks to bird populations.[38] Their classification as readily biodegradable highlights their potential for minimal environmental persistence, reducing the likelihood of long-term accumulation in ecosystems.[110] The low Bioconcentration Factor (BCF) value of 0.12 indicates negligible potential for bioaccumulation and biomagnification, supporting their environmental compatibility.[111] Moderate toxicity to Daphnia magna, with an LC_{50} value of 8.31($-\log10[(\text{mg L}^{-1})/(1000 \times \text{MW})]$), suggests some sensitivity in aquatic organisms, though the predicted impact on T. pyriformis (−16.4) suggests negligible microbial toxicity, indicating that basic aquatic microbial ecosystems may remain largely unaffected.[112] These findings suggest that **IPY 1** and **IPY 2** strike a favorable balance between biodegradability and low environmental persistence, with limited ecological risks under controlled use. Further experimental validation is recommended to confirm these findings and optimize their application in industrial settings.

6 Conclusion

In this study, two novel imidazo[1,2-*a*]pyrimidine-Schiff base derivatives (**IPY 1** and **IPY 2**) were synthesized and evaluated as corrosion inhibitors for mild steel in 1 M HCl solution. Electrochemical analyses (EIS, PDP) and weight loss measurements confirmed excellent inhibition efficiencies, exceeding 94% at 10^{-3} M. Surface characterization techniques (SEM, AFM, contact angle, FT-IR, UV–vis) supported the formation of a protective inhibitor layer on the steel surface. The adsorption of both inhibitors followed the Langmuir isotherm, with high K_{ads} values and negative ΔG_{ads}° indicating spontaneous, mixed-mode adsorption. Quantum chemical calculations and molecular simulations (DFT, MC, MD) provided further insight into the interaction mechanisms and supported the experimental findings. *In silico* toxicity assessments revealed favorable environmental and safety profiles for both compounds.

Overall, the results demonstrate that **IPY 1** and **IPY 2** are effective and environmentally friendly inhibitors, with **IPY 1** showing slightly stronger interaction with the metal surface. These findings offer valuable insights for the development of sustainable corrosion protection strategies.

Data availability

The datasets utilized and/or examined in the current study can be obtained from the corresponding author upon a reasonable request.

Author contributions

Mohamed Azzouzi: conceptualization, investigation, writing – original draft. Walid Daoudi: investigation, software, methodology. Omar Dagdag: formal analysis, methodology, writing. Hansang Kim: investigation, methodology. Avni Berisha: resources, review & editing. Abdelouahad Oussaid: methodology, formal analysis. Abdelmalik El Aatiaoui: validation, review & editing. Adyl Oussaid: supervision and validation.

Conflicts of interest

The authors have no relevant financial or non-financial interests to disclose.

Acknowledgements

This research was conducted with the support of the "Core Technology Development Project for New and Renewable Energy" by the Ministry of Trade, Industry and Energy (MOTIE) and the Korea Institute of Energy Technology Evaluation and Planning (KETEP) (No. RS-2024-00449107).

References

1 N. Arrousse, R. Salim, A. Abdellaoui, F. E. Hajjaji, B. Hammouti, E. H. Mabrouk, W. A. Diño and M. Taleb, *J. Taiwan Inst. Chem. Eng.*, 2021, **120**, 344–359.

2 A. R. Shahmoradi, N. Talebibahmanbigloo, A. A. Javidparvar, G. Bahlakeh and B. Ramezanzadeh, *J. Mol. Liq.*, 2020, **304**, 112751.
3 A. Lahhit, I. Azghay, A. Elyoussfi, M. Ghalit, Y. Ouzidan, M. E. Massaoudi, F. Mourabit, E. H. Akichouh, M. h. Ahari, H. Amhamdi and A. Salhi, *Environ. Sci. Pollut. Res.*, 2024, **31**, 63652–63670.
4 A. A. Sulaimon, P. I. Murungi, B. N. Tackie-Otoo, P. C. Nwankwo and M. A. Bustam, *Environ. Sci. Pollut. Res.*, 2023, **30**, 119309–119328.
5 K. Xhanari and M. Finšgar, *RSC Adv.*, 2016, **6**, 62833–62857.
6 D. Sharma, A. Thakur, M. K. Sharma, A. Bhardwaj, A. Sihmar, H. Dahiya, A. K. Sharma, A. Kumar, A. Berisha and H. Om, *Environ. Sci. Pollut. Res.*, 2024, 1–27.
7 O. R. Wamba-Tchio, M. Pengou, A.-L. Teillout, C. Baumier, I. M. Mbomekallé, P. De Oliveira, C. P. Nanseu-Njiki and E. Ngameni, *J. Electroanal. Chem.*, 2022, **919**, 116553.
8 V. Saraswat, R. Kumari and M. Yadav, *J. Phys. Chem. Solids*, 2022, **160**, 110341.
9 A. R. Shahmoradi, M. Ranjbarghanei, A. A. Javidparvar, L. Guo, E. Berdimurodov and B. Ramezanzadeh, *J. Mol. Liq.*, 2021, **338**, 116550.
10 H. Es-soufi, E. Berdimurodov, M. I. Sayyed and L. Bih, *Environ. Sci. Pollut. Res.*, 2024, 1–27.
11 R. Aslam, M. Mobin, S. Zehra and J. Aslam, *J. Mol. Liq.*, 2022, **364**, 119992.
12 M. A. Hegazy, A. M. Hasan, M. M. Emara, M. F. Bakr and A. H. Youssef, *Corros. Sci.*, 2012, **65**, 67–76.
13 E. J. Low, H. M. Yusoff, N. Batar, I. N. Z. Nor Azmi, P. W. Chia, S. S. Lam, S.-Y. Kan, R. K. Liew, G. E. Lee, K. Venkateswarlu and M. F. Ridwan Zulkifli, *Environ. Sci. Pollut. Res.*, 2023, **30**, 76297–76307.
14 X. Yang, F. Li and W. Zhang, *RSC Adv.*, 2019, **9**, 10454–10464.
15 C. Verma, A. Alfantazi, M. A. Quraishi and K. Y. Rhee, *Sustain. Chem. Pharm.*, 2023, **31**, 100943.
16 R. E. L. Adnani, O. Roby, B. Youbi, Y. Lghazi, A. Aynaou, K. Waderhman, S. Tighadouini, A. Y. A. Alzahrani, R. Saddik and I. Bimaghra, *Environ. Sci. Pollut. Res.*, 2024, **31**, 65661–65675.
17 A. Kosari, M. H. Moayed, A. Davoodi, R. Parvizi, M. Momeni, H. Eshghi and H. Moradi, *Corros. Sci.*, 2014, **78**, 138–150.
18 G. Wang, W. Li, X. Wang, X. Yuan and H. Yang, *Mater. Chem. Phys.*, 2023, **293**, 126956.
19 M. Gabsi, H. Ferkous, A. Delimi, A. Boublia, C. Boulechfar, A. Kahlouche, A. S. Darwish, T. Lemaoui and Y. Benguerba, *Environ. Sci. Pollut. Res.*, 2023, **30**, 59081–59105.
20 M. A. Ahmed, S. Amin and A. A. Mohamed, *RSC Adv.*, 2024, **14**, 31877–31920.
21 F. Kaya, R. Solmaz and İ. Halil Geçibesler, *J. Ind. Eng. Chem.*, 2023, **122**, 102–117.
22 W. Zhang, H. Li, Y. Wu, Q. Luo, H. Liu and L. Niu, *Chem. Res. Chin. Univ.*, 2018, **34**, 817–822.
23 Y. Di, X. Li, Z. Chen, X. Yin, Y. Chen, Y. Liu and W. Yang, *J. Mol. Struct.*, 2022, **1268**, 133737.
24 A. Chaouiki, M. Chafiq, M. Rbaa, H. Lgaz, R. Salghi, B. Lakhrissi, I. H. Ali, S. Masroor and Y. Cho, *Coatings*, 2020, 10.
25 W. Al Zoubi, S. G. Mohamed, A. A. S. Al-Hamdani, A. P. Mahendradhany and Y. G. Ko, *RSC Adv.*, 2018, **8**, 23294–23318.
26 L. Chen, D. Lu and Y. Zhang, *Materials*, 2022, 15.
27 K. Wan, P. Feng, B. Hou and Y. Li, *RSC Adv.*, 2016, **6**, 77515–77524.
28 M. Azzouzi, Z. E. Ouafi, O. Azougagh, W. Daoudi, H. Ghazal, S. E. Barkany, R. Abderrazak, S. Mazières, A. E. Aatiaoui and A. Oussaid, *J. Mol. Struct.*, 2023, **1285**, 135525.
29 W. Daoudi, A. El Aatiaoui, N. Falil, M. Azzouzi, A. Berisha, L. O. Olasunkanmi, O. Dagdag, E. E. Ebenso, M. Koudad, A. Aouinti, M. Loutou and A. Oussaid, *J. Mol. Liq.*, 2022, **363**, 119839.
30 T. Mao, H. Huang, D. Liu, X. Shang, W. Wang and L. Wang, *J. Mol. Liq.*, 2021, **339**, 117174.
31 N. Benachour, A. Delimi, H. Allal, A. Boublia, A. Sedik, H. Ferkous, A. Djedouani, S. Brioua, C. Boulechfar, H. Benzouid, A. Houssou, A. Oral, B. Ernst, M. Alam and Y. Benguerba, *RSC Adv.*, 2024, **14**, 12533–12555.
32 K. Zakaria, A. Hamdy, M. A. Abbas and O. M. Abo-Elenien, *J. Taiwan Inst. Chem. Eng.*, 2016, **65**, 530–543.
33 Y. Fernine, R. Salim, N. Arrousse, R. Haldhar, F. El Hajjaji, S.-C. Kim, M. Ebn Touhami and M. Taleb, *J. Mol. Liq.*, 2022, **355**, 118867.
34 C. Verma, I. B. Obot, I. Bahadur, E.-S. M. Sherif and E. E. Ebenso, *Appl. Surf. Sci.*, 2018, **457**, 134–149.
35 L. Gao, S. Peng, X. Huang and Z. Gong, *Appl. Surf. Sci.*, 2020, **511**, 145446.
36 M. Azzouzi, O. Dagdag, T. Rohand, H. Kim, A. Berisha, A. El Boutaybi, M. Abboud and A. Oussaid, *Inorg. Chem. Commun.*, 2024, **170**, 113273.
37 B. Yang, W. Yin, J. Yao, Q. Sheng and Z. Zhu, *Appl. Surf. Sci.*, 2022, **571**, 151177.
38 P. Banerjee, E. Kemmler, M. Dunkel and R. Preissner, *Nucleic Acids Res.*, 2024, **52**, W513–W520.
39 Y. Myung, A. G. C. de Sá and D. B. Ascher, *Nucleic Acids Res.*, 2024, **52**, W469–W475.
40 F. El-Hajjaji, R. A. Belkhmima, B. Zerga, M. Sfaira, M. Taleb, M. E. Touhami, B. Hammouti, S. S. Al-Deyab and E. Ebenso, *Int. J. Electrochem. Sci.*, 2014, **9**, 4721–4731.
41 M. Gopiraman, N. Selvakumaran, D. Kesavan, I. S. Kim and R. Karvembu, *Ind. Eng. Chem. Res.*, 2012, **51**, 7910–7922.
42 S. Dahiya, S. Lata, R. Kumar and O. S. Yadav, *J. Mol. Liq.*, 2016, **221**, 124–132.
43 A. Döner and G. Kardaş, *Corros. Sci.*, 2011, **53**, 4223–4232.
44 D. M. Gurudatt and K. N. Mohana, *Ind. Eng. Chem. Res.*, 2014, **53**, 2092–2105.
45 J. Zhang, X. L. Gong, H. H. Yu and M. Du, *Corros. Sci.*, 2011, **53**, 3324–3330.
46 H. Jafari, K. Akbarzade and I. Danaee, *Arab. J. Chem.*, 2019, **12**, 1387–1394.
47 A. Singh, Y. Lin, K. R. Ansari, M. A. Quraishi, E. E. Ebenso, S. Chen and W. Liu, *Appl. Surf. Sci.*, 2015, **359**, 331–339.

48 X. Ma, X. Jiang, S. Xia, M. Shan, X. Li, L. Yu and Q. Tang, *Appl. Surf. Sci.*, 2016, **371**, 248–257.
49 K. Berdimuradov, E. Berdimurodov, R. Haldhar, B. Lal, S.-C. Kim, L. Guo, G. K. Ziyayeva, K. P. Katin, N. Aliev and A. Hosseini-Bandegharaei, *Environ. Sci. Pollut. Res.*, 2024, **31**, 56499–56522.
50 K. K. Kumar, R. Brindha, M. Nandhini, M. Selvam, K. Saminathan and K. Sakthipandi, *Ionics*, 2019, **25**, 1699–1706.
51 H. M. Abd El-Lateef, K. Shalabi and A. H. Tantawy, *New J. Chem.*, 2020, **44**, 17791–17814.
52 A. Dehghani, G. Bahlakeh, B. Ramezanzadeh and M. Ramezanzadeh, *J. Mol. Liq.*, 2019, **279**, 603–624.
53 P. Dohare, M. A. Quraishi and I. B. Obot, *J. Chem. Sci.*, 2018, **130**, 8.
54 G. Khan, W. J. Basirun, S. N. Kazi, P. Ahmed, L. Magaji, S. M. Ahmed, G. M. Khan, M. A. Rehman and A. B. B. M. Badry, *J. Colloid Interface Sci.*, 2017, **502**, 134–145.
55 K. F. Khaled and N. Hackerman, *Electrochim. Acta*, 2003, **48**, 2715–2723.
56 X. Li, S. Deng and X. Xie, *Corros. Sci.*, 2014, **81**, 162–175.
57 A. O. Alnajjar, H. M. Abd El-Lateef, M. M. Khalaf and I. M. A. Mohamed, *Constr. Build. Mater.*, 2022, **317**, 125918.
58 B. J. Usman, S. A. Umoren and Z. M. Gasem, *J. Mol. Liq.*, 2017, **237**, 146–156.
59 M. Yadav, R. R. Sinha, S. Kumar and T. K. Sarkar, *RSC Adv.*, 2015, **5**, 70832–70848.
60 M. Mobin, M. Parveen and R. Aslam, *J. Phys. Chem. Solids*, 2022, **161**, 110422.
61 S. Kaya, B. Tüzün, C. Kaya and I. B. Obot, *J. Taiwan Inst. Chem. Eng.*, 2016, **58**, 528–535.
62 M. Ouakki, M. Galai, Z. Benzekri, Z. Aribou, E. Ech-chihbi, L. Guo, K. Dahmani, K. Nouneh, S. Briche, S. Boukhris and M. Cherkaoui, *J. Mol. Liq.*, 2021, **344**, 117777.
63 F. El-Hajjaji, E. Ech-chihbi, N. Rezki, F. Benhiba, M. Taleb, D. S. Chauhan and M. A. Quraishi, *J. Mol. Liq.*, 2020, **314**, 113737.
64 M. A. Quraishi, I. Ahamad, A. K. Singh, S. K. Shukla, B. Lal and V. Singh, *Mater. Chem. Phys.*, 2008, **112**, 1035–1039.
65 H. Didouh, A. Buyuksagis, M. h. Meliani, M. Dilek, Y. Kayali, R. K. Suleiman and T. A. Saleh, *J. Mol. Liq.*, 2023, **390**, 122910.
66 L. Guo, J. Tan, S. Kaya, S. Leng, Q. Li and F. Zhang, *J. Colloid Interface Sci.*, 2020, **570**, 116–124.
67 A. Biswas, S. Pal and G. Udayabhanu, *Appl. Surf. Sci.*, 2015, **353**, 173–183.
68 M. Oubaaqa, M. Ouakki, M. Rbaa, A. Elgendy, R. Idouhli, M. Maatallah, A. Jarid, M. E. Touhami, B. Lakhrissi and A. Zarrouk, *Mater. Today Commun.*, 2023, **35**, 106188.
69 S. Javadian, A. Yousefi and J. Neshati, *Appl. Surf. Sci.*, 2013, **285**, 674–681.
70 Y. Boughoues, M. Benamira, L. Messaadia and N. Ribouh, *Colloids Surf. A Physicochem. Eng. Asp.*, 2020, **593**, 124610.
71 F. Bentiss, M. Lebrini and M. Lagrenée, *Corros. Sci.*, 2005, **47**, 2915–2931.
72 A. Rahimi, A. Farhadian, A. Berisha, A. Shaabani, M. A. Varfolomeev, V. Mehmeti, X. Zhong, S. Yousefzadeh and R. Djimasbe, *Chem. Eng. J.*, 2022, **446**, 136938.
73 A. Singh, K. R. Ansari, D. S. Chauhan, M. A. Quraishi, H. Lgaz and I.-M. Chung, *J. Colloid Interface Sci.*, 2020, **560**, 225–236.
74 K. R. Ansari, D. S. Chauhan, M. A. Quraishi and T. A. Saleh, *J. Colloid Interface Sci.*, 2020, **564**, 124–133.
75 M. H. Shahini, M. Ramezanzadeh, G. Bahlakeh and B. Ramezanzadeh, *J. Mol. Liq.*, 2021, **332**, 115876.
76 M. Galai, K. Dahmani, O. Kharbouch, M. Rbaa, N. Alzeqri, L. Guo, A. A. AlObaid, A. Hmada, N. Dkhireche, E. Ech-chihbi, M. Ouakki, M. E. Touhami and I. Warad, *J. Phys. Chem. Solids*, 2024, **184**, 111681.
77 X.-L. Li, B. Xie, J.-S. Feng, C. Lai, X.-X. Bai, T. Li, D.-L. Zhang, W.-Y. Mou, L. Wen and Y.-T. Gu, *J. Mol. Liq.*, 2022, **345**, 117032.
78 X. Li, S. Deng and G. Du, *J. Taiwan Inst. Chem. Eng.*, 2022, **131**, 104171.
79 V. Saraswat and M. Yadav, *Colloids Surf. A Physicochem. Eng. Asp.*, 2021, **627**, 127172.
80 Q. H. Zhang, B. S. Hou, Y. Y. Li, G. Y. Zhu, H. F. Liu and G. A. Zhang, *J. Colloid Interface Sci.*, 2021, **585**, 355–367.
81 R. K. Mehta, S. K. Gupta and M. Yadav, *J. Environ. Chem. Eng.*, 2022, **10**, 108499.
82 G. Bahlakeh, B. Ramezanzadeh, A. Dehghani and M. Ramezanzadeh, *J. Mol. Liq.*, 2019, **283**, 174–195.
83 I. A. Hermoso-Diaz, A. E. Foroozan, J. P. Flores-De los Rios, L. L. Landeros-Martinez, J. Porcayo-Calderon and J. G. Gonzalez-Rodriguez, *J. Mol. Struct.*, 2019, **1197**, 535–546.
84 H. Shokry, *J. Mol. Struct.*, 2014, **1060**, 80–87.
85 H. Lgaz, I.-M. Chung, R. Salghi, I. H. Ali, A. Chaouiki, Y. El Aoufir and M. I. Khan, *Appl. Surf. Sci.*, 2019, **463**, 647–658.
86 N. El-Aouni, O. Dagdag, A. El Amri, H. Kim, A. Elbachiri, E. Berdimurodov, A. Berisha, M. Rafik and N. Aliev, *Colloids Surf. A Physicochem. Eng. Asp.*, 2024, **690**, 133730.
87 M. E. Belghiti, S. Echihi, A. Dafali, Y. Karzazi, M. Bakasse, H. Elalaoui-Elabdallaoui, L. O. Olasunkanmi, E. E. Ebenso and M. Tabyaoui, *Appl. Surf. Sci.*, 2019, **491**, 707–722.
88 B. Liu, H. Xi, Z. Li and Q. Xia, *Appl. Surf. Sci.*, 2012, **258**, 6679–6687.
89 Y. Ma, B. Fan, H. Liu, G. Fan, H. Hao and B. Yang, *Appl. Surf. Sci.*, 2020, **514**, 146086.
90 G. Wang, W. Li, X. Wang, S. Fan and H. Yang, *Appl. Surf. Sci.*, 2023, **638**, 157946.
91 H. Lgaz and H.-s. Lee, *Appl. Surf. Sci.*, 2024, **644**, 158763.
92 M. Alahiane, R. Oukhrib, Y. Ait Albrimi, H. Abou Oualid, R. Idouhli, A. Nahlé, A. Berisha, N. Z. Azzallou and M. Hamdani, *Appl. Surf. Sci.*, 2023, **612**, 155755.
93 W. Li, B. Tan, S. Zhang, L. Guo, J. Ji, M. Yan and R. Wang, *Appl. Surf. Sci.*, 2022, **602**, 154165.
94 H. Liu, Y. Lin, Q. Luo, W. Xu, J. He, B. Bao, Y. Xu, B. Zeng, C. Yuan, G. Chen and L. Dai, *Appl. Surf. Sci.*, 2024, **648**, 159069.
95 A. Ouass, M. Galai, M. Ouakki, E. Ech-Chihbi, L. Kadiri, R. Hsissou, Y. Essaadaoui, A. Berisha, M. Cherkaoui,

A. Lebkiri and E. H. Rifi, *J. Appl. Electrochem.*, 2021, **51**, 1009–1032.
96 M. Goyal, S. Kumar, I. Bahadur, C. Verma and E. E. Ebenso, *J. Mol. Liq.*, 2018, **256**, 565–573.
97 R. Haldhar, S.-C. Kim, A. Berisha, V. Mehmeti and L. Guo, *J. Adhes. Sci. Technol.*, 2023, **37**, 842–857.
98 A. El Aatiaoui, W. Daoudi, A. El Boutaybi, L. Guo, N.-E. Benchat, A. Aouinti, A. Oussaid and M. Loutou, *J. Mol. Liq.*, 2022, **350**, 118458.
99 A. E. L. Aatiaoui, M. Koudad, T. Chelfi, S. Erkan, M. Azzouzi, A. Aouniti, K. SavaŞ, M. Kaddouri, N. Benchat and A. Oussaid, *J. Mol. Struct.*, 2021, **1226**, 129372.
100 A. Elyoussfi, I. Azghay, S. Dadou, W. Daoudi, M. h. Ahari, H. Amhamdi, N. Benchat, A. E. Aatiaoui, A. Salhi and A. Dafali, *J. Mol. Struct.*, 2023, **1291**, 136025.
101 W. Daoudi, B. El Ibrahimi, O. Dagdag, E. Berdimurodov, L. Guo, E. E. Ebenso, A. Oussaid and A. El Aatiaoui, *J. Phys. Chem. Solids*, 2023, **179**, 111409.
102 W. Daoudi, M. Azzouzi, O. Dagdag, A. El Boutaybi, A. Berisha, E. E. Ebenso, A. Oussaid and A. El Aatiaoui, *Mater. Sci. Eng. B*, 2023, **290**, 116287.
103 J. S. Akhila, D. Shyamjith and M. Alwar, *Curr. Sci.*, 2007, **93**, 917–920.
104 F. Madia, G. Pillo, A. Worth, R. Corvi and P. Prieto, *Arch. Toxicol.*, 2021, **95**, 1971–1993.
105 S. Choudhuri, G. W. Patton, R. F. Chanderbhan, A. Mattia and C. D. Klaassen, *Toxicol. Sci.*, 2017, **161**, 5–22.
106 L. Moukheiber, W. Mangione, M. Moukheiber, S. Maleki, Z. Falls, M. Gao and R. Samudrala, 2022, **27**, 3021.
107 K. Goyal, H. Goel, P. Baranwal, A. Dixit, F. Khan, N. K. Jha, K. K. Kesari, P. Pandey, A. Pandey, M. Benjamin, A. Maurya, V. Yadav, R. S. Sinh, P. Tanwar, T. K. Upadhyay and S. Mittan, *Environ. Sci. Pollut. Res.*, 2022, **29**, 61993–62013.
108 Q. Wu, H. Liu, R. Zhang, X. Zhang and P. Xia, *Front. Endocrinol.*, 2024, 15.
109 J. N. Meyer, J. H. Hartman and D. F. Mello, *Toxicol. Sci.*, 2018, **162**, 15–23.
110 J. J. Ortega-Calvo, F. Stibany, K. T. Semple, A. Schaeffer, J. R. Parsons and K. E. C. Smith, in *Bioavailability of Organic Chemicals in Soil and Sediment*, ed. J. J. Ortega-Calvo and J. R. Parsons, Springer International Publishing, Cham, 2020, pp. 243–265, DOI: **10.1007/698_2020_586**.
111 D. Mackay, A. K. D. Celsie, D. E. Powell and J. M. Parnis, *Environ. Sci.:Processes Impacts*, 2018, **20**, 72–85.
112 F. Luan, T. Wang, L. Tang, S. Zhang and M. Natália Dias Soeiro Cordeiro, *Molecules*, 2018, **23**, 1002.